POLITECNICO DI TORINO

Corso di Laurea Magistrale
in Ingegneria Matematica

Tesi di Laurea Magistrale

Laminar–Turbulent Transition in Optimized and Deterministic Transport Networks

Supervisors
prof. Luca Ridolfi
prof. Amilcare Porporato

Candidate
Francesco Matteazzi

Academic Year 2025-2026

Abstract

This thesis investigates laminar–turbulent transitions in branching transport networks within a unified graph-based hydraulic framework. The central objective is to understand how regime changes, controlled by local Reynolds numbers, propagate through network architectures and how they affect global transport performance.

Two complementary classes of networks are considered. First, optimized transport networks (OTNs) are obtained by minimizing a global cost functional balancing hydraulic dissipation and maintenance expenditure. The constitutive pressure–flow relation allows for fully laminar, fully turbulent and mixed configurations, where the exponent is assigned edgewise according to a Reynolds threshold. Numerical experiments show that the onset of turbulence is hierarchical: it consistently appears on high-flow, large-radius edges and propagates downstream as demand increases.

Second, deterministic binary trees are analyzed as analytically tractable reference systems with prescribed geometry. Explicit scaling laws are derived for Reynolds number, pressure drop, and wall shear stress across generations, clarifying under which conditions turbulence emerges first at proximal or distal levels. In mixed configurations, laminar and turbulent subtrees coexist and contribute additively to the total head loss through linear and quadratic terms in the inlet discharge. This structure naturally leads to an equivalent single-pipe representation with a Moody-type friction law and to the definition of a dimensionless mixed resistance quantifying the relative weight of the two regimes.

By combining adaptive and prescribed architectures within the same hydraulic formulation, the thesis provides a coherent picture of laminar–turbulent transitions in networks, separating the roles of local flow physics, branching geometry, and structural optimization in shaping global transport behavior.

Contents

List of Tables 4

List of Figures 5

Introduction 7
Objectives . . . 8
Thesis outline . . . 8

1 Mathematical Model 9
1.1 Graph formulation . . . 9
1.2 Constitutive law . . . 10
1.3 Flow regimes and regime exponents . . . 10
1.4 Flow regimes considered . . . 12
1.5 Derived fields . . . 13
1.6 Scope of the model . . . 13

I Optimized Transport Networks (OTNs) 15

2 Optimization Framework 17
2.1 Cost Functional . . . 17
2.2 Maintenance models . . . 18
2.3 Remarks on modeling closures . . . 20

3 Numerical Methods and Experimental Design 23
3.1 Domain and forcing . . . 23
3.2 Optimization Algorithm . . . 23
3.3 Post-processing metrics . . . 25
3.3.1 Statistical analysis of distributions . . . 26
3.4 Demand sweep protocols . . . 27
3.4.1 Setup of the sweep . . . 27
3.4.2 Two sweep protocols: re-optimized vs rigid sweep . . . 27
3.4.3 Turbulent fraction . . . 28
3.4.4 Equivalent resistance . . . 28

4 Numerical Results on OTNs 31
4.1 Convergence and optimization traces . . . 32
4.2 Topology and edge fields . . . 35
4.3 Statistical distributions . . . 39
4.4 Laminar–turbulent transition under increasing demand . . . 45
4.4.1 Re-optimized sweep . . . 45
4.4.2 Fixed-radii sweep . . . 48
4.5 Discussion . . . 50

II Deterministic Binary Trees **53**

5 Deterministic binary tree model 55
5.1 Geometry and scaling . . . 55
5.2 Hydraulic scalings along the tree . . . 56
5.2.1 Reynolds number and flow regimes . . . 56
5.2.2 Level-wise head losses and global decomposition . . . 57
5.2.3 Wall shear stress scalings . . . 58
5.3 Equivalent pipe representation . . . 59
5.4 Equivalent friction factor . . . 60
5.5 Dimensionless mixed resistance . . . 60

6 Numerical Results on Deterministic Binary Trees 63
6.1 Setup of the numerical sweep . . . 63
6.2 Local flow fields and global descriptors . . . 64
6.3 Discussion . . . 65

Conclusions 67
Optimized transport networks . . . 67
Deterministic binary trees . . . 68
Perspective and limitations . . . 68

List of Tables

4.1 Model, regime, and optimization parameters 32
4.2 Scaling exponents of the global distributions 45
4.3 Parameters used in the mixed laminar/turbulent sweep 46
4.4 Parameters used in the rigid sweep after one laminar optimization 48

List of Figures

1.1 Moody diagram . . . 11
2.1 Edgewise dissipation, maintenance and total cost . . . 19
2.2 Maintenance cost for different constant values of γ . . . 20
2.3 τ_w as a function of Re for laminar and fully developed turbulent closures . . . 21
3.1 Initialized conductances . . . 24
4.1 Evolution of total cost and dissipation during optimization for different regimes and maintenance models . . . 33
4.2 Mean and coefficient of variation of Reynolds number during optimization iterations . . . 34
4.3 Mean and coefficient of variation of wall shear stress during optimization iterations . . . 34
4.4 Optimal network configurations for different hydraulic regimes and maintenance models . . . 36
4.5 Optimal networks with edges colored by Reynolds number . . . 37
4.6 Optimal networks with edges colored by wall shear stress . . . 38
4.7 Flow distributions for optimized networks with constant maintenance exponent $\gamma = \frac{1}{2}$ . . . 41
4.8 Flow distributions for optimized networks with flow-dependent maintenance exponent $\gamma(Q)$ . . . 41
4.9 Reynolds number distributions for optimized networks with constant maintenance exponent . . . 42
4.10 Reynolds number distributions for optimized networks with flow-dependent maintenance exponent . . . 42
4.11 Wall shear stress distributions for optimized networks with constant maintenance exponent . . . 43
4.12 Wall shear stress distributions for optimized networks with flow-dependent maintenance exponent . . . 43
4.13 Equivalent radius distributions for optimized networks with constant maintenance exponent . . . 44
4.14 Equivalent radius distributions for optimized networks with flow-dependent maintenance exponent . . . 44
4.15 Spatial distribution of laminar and turbulent edges at increasing demand . . . 46
4.16 Turbulent fraction versus normalized demand for different grid sizes . . . 47
4.17 Equivalent resistance versus normalized demand for different grid sizes . . . 47

4.18 Spatial distribution of laminar and turbulent edges at increasing demand for fixed-radii networks . . . 49
4.19 Turbulent fraction versus normalized demand for fixed-radius networks . . 49
4.20 Equivalent resistance versus normalized demand for fixed-radius networks . 50
6.1 Local Reynolds number and wall shear stress along the binary tree for increasing inlet Reynolds number . . . 64
6.2 Global equivalent descriptors . . . 65

Introduction

Transport networks are ubiquitous in natural and engineered systems. They arise whenever a conserved quantity, such as mass, energy or information, must be distributed from sources to sinks through a spatially embedded structure. Examples range from river basins and vascular networks to distribution systems such as pipelines and power grids. Despite their diversity, many of these systems share common structural features, most notably hierarchical branching, flow heterogeneity and scaling laws.

From a modeling perspective, transport networks can be naturally represented as graphs whose edges carry flows and whose nodes act as junctions, sources or sinks. Within this framework, the organization of the network results from the interplay between global constraints (such as mass conservation), local constitutive laws linking flow and pressure drop, and, when adaptation is allowed, optimization principles reflecting energetic or structural costs.

A central question in the study of transport networks concerns the emergence of their topology. In particular, one may ask under which conditions optimal networks develop tree-like structures, characterized by a single path between any pair of nodes, or instead exhibit loops and redundancy. Previous work has shown that this dichotomy can often be traced back to the concavity or convexity of the cost associated with maintaining transport capacity [Banavar et al., 2000]. This connection between cost concavity and network topology has been extensively discussed in the context of optimal transport and biological networks. When maintenance costs scale sublinearly with conductance, transport tends to concentrate onto a reduced set of edges, favoring tree-like architectures. Conversely, superlinear costs promote the distribution of flow across multiple paths and the formation of loops.

Beyond topology, the physical regime governing flow along the network edges plays a crucial role. In fluid transport systems, the relation between pressure drop and flow rate depends on whether the flow is laminar or turbulent. Laminar flow is characterized by a linear pressure–flow relation, while turbulent flow introduces nonlinearity. In spatially heterogeneous networks, different edges may operate in different regimes, leading to mixed laminar–turbulent configurations. Understanding how these local regimes interact with global optimization principles remains an open and largely unexplored problem.

This thesis investigates transport networks from two complementary perspectives. On the one hand, we study *optimized transport networks* (OTNs), whose structure emerges from the minimization of a global cost functional balancing hydraulic dissipation and maintenance costs. On the other hand, we analyze *deterministic binary trees*, idealized

branching networks with prescribed geometry that allow for explicit analytical treatment. By employing a unified graph-based hydraulic framework, the thesis aims to isolate the respective roles of topology, constitutive flow laws, and optimization in shaping network structure and performance.

Objectives

The main objectives of this thesis are the following:

- To formulate a unified graph-based model for fluid transport networks, incorporating both linear (laminar) and nonlinear (turbulent) constitutive laws.
- To construct optimized transport networks through the minimization of a global cost functional and to compare the resulting structures across laminar, turbulent, and mixed hydraulic regimes.
- To characterize optimized networks using local and global diagnostic quantities, including Reynolds number, wall shear stress, equivalent radius, and statistical distributions thereof.
- To analyze deterministic binary trees as analytically tractable reference systems, deriving scaling laws for flow, wall shear stress, and global resistance under laminar, turbulent, and mixed regimes.
- To establish qualitative and quantitative connections between optimized transport networks and deterministic trees, clarifying which features arise from optimization and which are primarily controlled by geometry and flow physics.

Thesis outline

The thesis is organized as follows.

Chapter 1 introduces the general graph-based formulation of transport networks, including mass conservation, constitutive pressure–flow relations and the definition of diagnostic quantities common to all settings considered.

Part I is devoted to optimized transport networks. After presenting the optimization framework and numerical methods, we report and discuss numerical results on network topology, statistical properties, and laminar–turbulent transitions under increasing demand.

Part II focuses on deterministic binary trees. Analytical derivations of hydraulic scalings and equivalent resistance measures are developed and complemented by numerical simulations that explore mixed-regime behavior.

Finally, the Conclusions summarize the main findings, assess the achievements of the thesis with respect to its initial objectives and outline possible directions for future research.

Chapter 1

Mathematical Model

We consider networks of conduits carrying an incompressible fluid. Within this unified framework, two classes of networks are investigated in this thesis: *optimized transport networks*, whose structure emerges from the minimization of a prescribed cost functional, and *deterministic binary trees*, whose geometry is fixed *a priori* and analyzed analytically and numerically. The present chapter introduces the general flow equations and constitutive laws that are common to both settings. Optimization principles and cost functionals are introduced only where specifically required.

1.1 Graph formulation

Let $\mathcal{G} = (\mathcal{V}, \mathcal{E})$ be a directed network, where $\mathcal{V}$ denotes the set of vertices and $\mathcal{E}$ the set of edges, with $N = |\mathcal{V}|$. Each edge $(i, j) \in \mathcal{E}$ represents a physical conduit of length L_{ij} (e.g. a pipe or channel segment) connecting two nodes and carrying a volumetric flow rate Q_{ij}. The scalar C_{ij} denotes the hydraulic conductance of the edge, accounting for both geometric properties and material or frictional effects.

Each node $i \in \mathcal{V}$ is associated with a scalar pressure P_i, and edges transport flow in response to pressure differences between adjacent nodes. Vertices represent junctions where flows merge or split, as well as locations where external forcing is applied through nodal source terms s_i, with $s_i > 0$ denoting injection (source) and $s_i < 0$ withdrawal (sink).

The only global constraint imposed on the network is mass conservation,

$$\sum_{i \in \mathcal{V}} s_i = 0, \tag{1.1}$$

which ensures that the total injection balances the total withdrawal. At the local level, mass conservation requires that, at each node, the sum of incoming and outgoing fluxes balances the external source or sink term. Different choices of the source–sink configuration, including drainage networks with distributed sinks or purely conservative transport, will be specified later when discussing particular network realizations. Accordingly, mass

conservation at node i reads

$$\sum_{j \in \mathcal{N}_i^+} Q_{ij} \; - \; \sum_{k \in \mathcal{N}_i^-} Q_{ki} \; = \; s_i \qquad \forall i, \tag{1.2}$$

where $\mathcal{N}_i^+ = \{\, j \in \mathcal{V} : (i,j) \in \mathcal{E} \,\}$ is the set of out-neighbors of node i and $\mathcal{N}_i^- = \{\, k \in \mathcal{V} : (k,i) \in \mathcal{E} \,\}$ is its set of in-neighbors.

1.2 Constitutive law

Flow along each edge is driven by a pressure difference between its endpoints. We assume that the volumetric flow rate Q_{ij} depends on the pressure drop $\Delta P_{ij} = P_i - P_j$ through a generalized constitutive relation of the form

$$Q_{ij} = C_{ij} \, (\Delta P_{ij})^{\alpha_{ij}}. \tag{1.3}$$

Here C_{ij} is the hydraulic conductance of edge (i,j), which quantifies the ease with which fluid can be transported through the conduit. The exponent α_{ij} encodes the local flow regime: $\alpha_{ij} = 1$ corresponds to linear (laminar) behavior, while $\alpha_{ij} < 1$ captures nonlinear dissipation characteristic of turbulent flow. The specific values of α corresponding to laminar and turbulent closures are derived in the next section.

1.3 Flow regimes and regime exponents

The exponent α appearing in the constitutive law has a clear physical interpretation: it summarizes how dissipative losses scale with flow intensity. Different values of α correspond to distinct hydraulic regimes and arise from different friction mechanisms acting at the conduit walls.

Here we derive the regime-dependent pressure–flow relations starting from the Darcy–Weisbach formulation for head losses in conduits. Let $D_{ij} = 2\, r_{ij}$ denote the hydraulic diameter of edge (i,j), U_{ij} the mean flow velocity, and γ_f the specific weight of the fluid. Dropping subscripts for simplicity, the Darcy–Weisbach relation reads

$$f \; = \; \frac{2\, g\, D}{U^2} \, \frac{\Delta P}{L\, \gamma_f}, \tag{1.4}$$

where f is the Darcy friction factor. Its dependence on the Reynolds number $Re = UD/\nu$ is given, in the regimes considered here, by the classical scalings

$$f = \frac{64}{Re} \qquad \text{(laminar)}, \tag{1.5}$$

$$f = 0.316\, Re^{-0.25} \qquad \text{(turbulent, smooth walls)}, \tag{1.6}$$

$$f = \text{const.} \qquad \text{(turbulent, rough walls)}. \tag{1.7}$$

These classical scalings correspond to the main branches of the Moody diagram, which summarizes the dependence of the Darcy friction factor on the Reynolds number and

on the relative wall roughness. In particular, the laminar regime is characterized by a universal $f \sim Re^{-1}$ decay, independent of surface properties, while turbulent flows exhibit qualitatively different behaviors depending on whether viscous or roughness effects dominate near the wall.

This distinction is crucial for the present work, as it motivates the use of different constitutive exponents in the pressure–flow relation. Figure 1.1 provides a representation of the aforementioned Moody diagram. To relate these expressions to the constitutive law

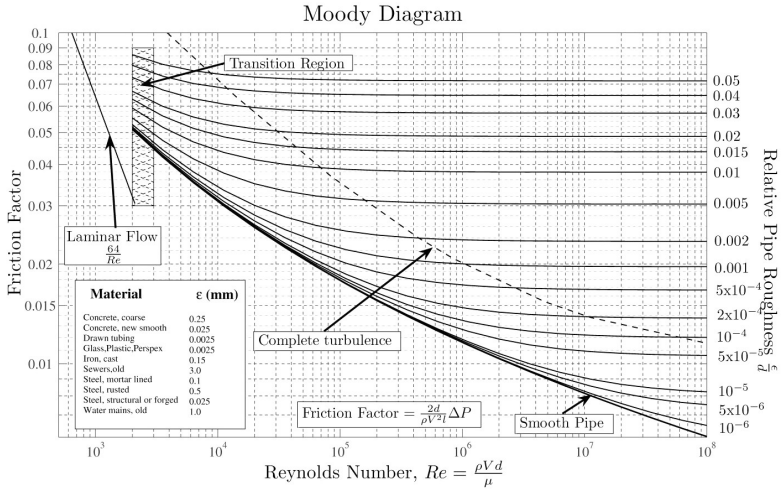

Figure 1.1: Schematic Moody diagram showing the dependence of the Darcy friction factor f on the Reynolds number Re for different wall roughnesses.

(1.3), we rewrite (1.4) as

$$\Delta P = \frac{f\, U^2\, L\, \gamma_f}{2\, g\, D}. \tag{1.8}$$

Assuming cylindrical conduits, the flow rate is

$$Q = U\, A = U\, \frac{\pi D^2}{4} \qquad \Longrightarrow \qquad U = \frac{4Q}{\pi D^2},$$

which substituted into (1.8) yields

$$\Delta P = \frac{8\, f\, Q^2\, L\, \gamma_f}{g\, D^5\, \pi^2}. \tag{1.9}$$

Let's first consider the laminar case. Using (1.5), the friction factor can be written as

$$f = \frac{64}{Re} = \frac{64\, \nu}{U D} = \frac{16\, \nu\, \pi D}{Q}. \tag{1.10}$$

Substitution into (1.9) gives

$$\Delta P = \frac{128\, \nu\, L\, \gamma_f}{g\, \pi\, D^4}\, Q = \frac{Q}{C}, \tag{1.11}$$

showing that, in the laminar regime, the pressure drop is proportional to the flow rate and the constitutive exponent is $\alpha = 1$.

Proceeding analogously for the turbulent scalings of Eqs. (1.6)-(1.7), one obtains the regime exponents

$$\alpha = 1 \quad \text{(laminar)}, \qquad \alpha = \tfrac{4}{7} \quad \text{(turbulent, smooth walls)}, \qquad \alpha = \tfrac{1}{2} \quad \text{(turbulent, rough walls)}.$$

In fully laminar or fully turbulent scenarios, the exponent α is uniform over the entire network and reflects a single dominant dissipation mechanism. The Reynolds number thus provides a natural criterion to identify the appropriate constitutive regime by quantifying the balance between viscous and inertial effects in each conduit.

In mixed laminar–turbulent configurations, however, different flow regimes may coexist across the network. In this case, the constitutive exponent α_{ij} is assigned edgewise according to the local Reynolds number on each conduit, leading to a heterogeneous network in which linear and nonlinear pressure–flow relations coexist. This edgewise classification forms the basis for the mixed-regime scenarios analyzed throughout this work.

1.4 Flow regimes considered

We consider three hydraulic regimes that differ only in the assignment of the constitutive exponent α on the network edges.

Fully laminar regime. All edges operate in the laminar regime and are assigned a uniform exponent $\alpha = 1$. This setting corresponds to classical Poiseuille flow and represents the baseline configuration. Laminar optimal networks have been previously studied in Giaccone et al. [2025]; here this regime is revisited within a unified framework and systematically compared with the turbulent and mixed cases.

Fully developed turbulent regime. All edges operate in fully developed turbulent flow on rough walls and are assigned a uniform exponent $\alpha = \frac{1}{2}$, consistent with the Reynolds-independent friction factor scaling in Eq. (1.7). This choice isolates the effect of nonlinear dissipation on network structure and transport properties.

Mixed laminar–turbulent regime. In the mixed configuration, the flow regime is assigned *edgewise* according to the local Reynolds number Re_{ij}. The constitutive exponent switches as

$$\text{laminar if } Re_{ij} \leq Re_c, \qquad \text{fully developed turbulent if } Re_{ij} > Re_c,$$

where Re_c is a fixed critical threshold.

In the simulations presented in this thesis, a critical threshold Re_c is introduced to discriminate between laminar and turbulent regimes in mixed configurations. The threshold Re_c used later in the simulations should not be interpreted as the physical onset of turbulence in a single pipe; rather, it plays the role of a modeling parameter, chosen so as to allow the coexistence of laminar and turbulent branches under the adopted parameters.

Edgewise assignments of different hydraulic regimes based on local Reynolds numbers have been previously considered in both biological and engineered transport networks.

1.5 Derived fields

In addition to the primary variables (Q_{ij}, ΔP_{ij}, C_{ij}), several derived fields are introduced to characterize the hydraulic state of the network and to enable quantitative comparisons between different regimes.

Reynolds number. The local Reynolds number associated with edge (i, j) is defined as

$$Re_{ij} = \frac{U_{ij} D_{ij}}{\nu} = \frac{4\, Q_{ij}}{\pi\, \nu\, D_{ij}}, \tag{1.12}$$

where $D_{ij} = 2r_{ij}$ is the hydraulic diameter and ν is the kinematic viscosity of the fluid. The Reynolds number is used both as a diagnostic quantity and, in the mixed regime, as the criterion for assigning the local constitutive exponent α_{ij}.

Wall shear stress. The wall shear stress acting on edge (i, j) is defined as

$$\tau_{w,ij} = \frac{r_{ij}}{2} \frac{\Delta P_{ij}}{L_{ij}}, \tag{1.13}$$

which follows directly from the balance between pressure forces and wall friction in a cylindrical conduit.

Equivalent radius. To facilitate physical interpretation, it is convenient to associate each edge with an equivalent cylindrical conduit whose radius reproduces the same conductance under the adopted constitutive law. An equivalent hydraulic radius r_{ij} is thus inferred from the conductance C_{ij} by inverting the corresponding constitutive relation. In the laminar regime, using Eq. (1.11), one obtains

$$r_{ij} = \left(\frac{8\, \mu\, L_{ij}\, C_{ij}}{\pi} \right)^{1/4}. \tag{1.14}$$

In the fully rough turbulent flow, the equivalent radius reads

$$r_{ij} = \left(\frac{f\, \gamma_f\, L_{ij}\, C_{ij}^2}{4\pi\, g} \right)^{1/3}. \tag{1.15}$$

1.6 Scope of the model

The formulation introduced in this chapter provides a unified description of flow on networks under different hydraulic regimes. In the remainder of the thesis, this framework is specialized to two distinct settings. In Part I, it is applied to optimized transport networks, where conductances emerge from the minimization of a cost functional. In Part II, the same flow laws and diagnostic quantities are employed to analyze deterministic binary trees with prescribed geometry.

Part I

Optimized Transport Networks (OTNs)

Chapter 2

Optimization Framework

Optimized transport networks (OTNs) are networked systems whose structure emerges from the competition between transport efficiency and the cost of building and maintaining the network itself. Rather than prescribing the geometry *a priori*, the network topology is obtained by minimizing a global cost functional under flow-conservation constraints.

This modeling approach has been widely used to describe transport systems in natural and engineered settings, including vascular networks and river basins.

In this part of the thesis, optimized transport networks are constructed by solving a variational problem that balances hydraulic dissipation against maintenance costs. This optimization framework is introduced here and will be used throughout Part I to generate and analyze OTNs under different flow regimes and maintenance models.

2.1 Cost Functional

In order to model the emergence of optimal transport architectures, we introduce a variational principle that assigns a global cost to a given network configuration. Physically, the cost functional J represents a balance between the energetic expenditure required to transport fluid through the network and the structural investment needed to build and maintain the conduits. It is not intended as a fundamental physical law, but as an effective modeling principle capturing the trade-off between energetic efficiency and structural investment.

For a given assignment of conductances $\{C_{ij}\}$ and flows $\{Q_{ij}\}$, the total network cost is defined as

$$J = J^{(D)} + J^{(\gamma)} = \sum_{(i,j)\in\mathcal{E}} \left(\frac{Q_{ij}^{(1+\alpha_{ij})/\alpha_{ij}}}{C_{ij}^{1/\alpha_{ij}}} \; + \; b\, C_{ij}^{\gamma(Q_{ij})} \right), \tag{2.1}$$

where the summation extends over all admissible edges of the underlying graph. Cost functionals of the form (2.1), balancing dissipation and maintenance costs, are widely used to model adaptive transport networks and vascular architectures. In particular, formulations of this type are known to be equivalent to other variational principles proposed in literature for the generation of optimized transport networks [Lu and Kou, 2022].

The optimization problem consists in minimizing J with respect to the conductances $\{C_{ij}\}$. For a given conductance field, the flows $\{Q_{ij}\}$ and nodal pressures are implicitly determined by the mass-conservation constraints and by the constitutive relation (1.3).

Dissipation term. The first contribution $J^{(D)}$ represents the hydraulic power dissipated along each edge. The mechanical power loss on edge (i, j) reads

$$\mathcal{P}_{w,ij} = Q_{ij}\,\Delta P_{ij}, \tag{2.2}$$

and, using the constitutive law (1.3), it can be written as

$$\mathcal{P}_{w,ij} = Q_{ij}\left(\frac{Q_{ij}}{C_{ij}}\right)^{1/\alpha_{ij}} = \frac{Q_{ij}^{(1+\alpha_{ij})/\alpha_{ij}}}{C_{ij}^{1/\alpha_{ij}}}. \tag{2.3}$$

This term penalizes large pressure drops and inefficient flow distributions, thus promoting energetically efficient transport configurations.

Maintenance term. The maintenance term accounts for energetic, material, or biological costs associated with sustaining a conduit of given conductance, including construction, repair, and metabolic expenditure. The contribution $J^{(\gamma)}$ therefore represents the structural investment required to maintain an edge in the network. The coefficient $b > 0$ controls the relative importance of maintenance with respect to dissipation.

Fig. 2.1 schematizes the two competing contributions $J^{(D)}$ and $J^{(\gamma)}$ for a single edge as a function of its conductance, at fixed flow. While dissipation decreases with increasing conductance, maintenance costs grow, and their balance selects a finite optimal value of C.

The resulting variational problem can be written as

$$\begin{aligned} \min_{\{C_{ij}\geq 0\}} \quad & J(C) \\ \text{s.t.} \quad & \sum_{j\in\mathcal{N}_i^+} Q_{ij} - \sum_{k\in\mathcal{N}_i^-} Q_{ki} = s_i \qquad \forall i \in \mathcal{V}, \\ & Q_{ij} = C_{ij}\,(\Delta P_{ij})^{\alpha_{ij}} \qquad \forall (i,j) \in \mathcal{E}. \end{aligned} \tag{2.4}$$

The optimization problem consists in finding a conductance field $C = \{C_{ij}\}$ that minimizes the total cost J, while flows and pressures are implicitly determined by the flow equations.

2.2 Maintenance models

The exponent γ controls how construction and maintenance costs scale with the conductance of a single edge and thus determines how expensive it is, from a structural standpoint, to sustain large transport capacities. Its value plays a key role in determining the large-scale topology of the optimized network.

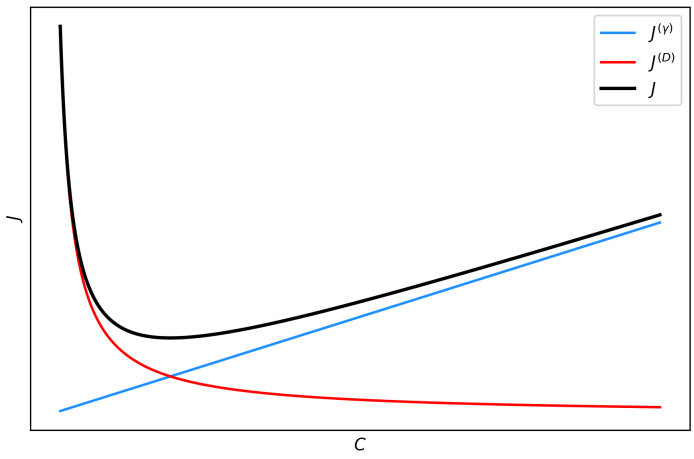

Figure 2.1: Edgewise cost contributions as a function of the conductance C for a fixed flow Q. $J^{(D)}$ decreases with increasing C, while $J^{(\gamma)}$ increases. The total cost $J = J^{(D)} + J^{(\gamma)}$ therefore exhibits a well-defined minimum, which determines the optimal conductance for the edge.

Constant maintenance exponent. When γ is constant, the maintenance contribution $J^{(\gamma)}$ is a concave function of C for $\gamma < 1$. In this case, the cost functional favors the concentration of transport into a reduced number of highly conductive edges, leading to tree-like optimal structures without loops. This regime is typically associated with branched transport networks.

Conversely, for $\gamma > 1$ the maintenance term is convex and penalizes large conductances. As a result, transport is distributed over multiple alternative paths, and the optimal configuration exhibits loops and redundancy. The value $\gamma = 1$ marks a neutral case separating these two behaviors [Banavar et al., 2000].

This behavior is illustrated in Fig. 2.2, which shows the maintenance cost $J^{(\gamma)}$ associated with a single edge as a function of its conductance, for different values of constant exponent γ.

This qualitative transition between tree-like and loopy architectures as a function of the maintenance exponent has been reported in several optimization studies.

Flow-dependent maintenance exponent. In addition to constant choices, we also consider a flow-dependent maintenance exponent $\gamma(Q)$, which allows different scaling behaviors to coexist within the same network. This generalization enables a smooth transition between tree-like and loopy structures as a function of the local flow intensity.

Following Giaccone et al. [2025], we adopt a flow-dependent maintenance exponent

$$\gamma(Q) = 1 - \frac{\delta}{2} \tanh(Q - Q_{\min} - \ell\,(Q_{\max} - Q_{\min}))\,, \tag{2.5}$$

where $Q_{\min}$ and $Q_{\max}$ are the minimum and maximum flow rates in the network. The parameter $\delta > 0$ controls the amplitude of the transition between tree-favoring ($\gamma < 1$)

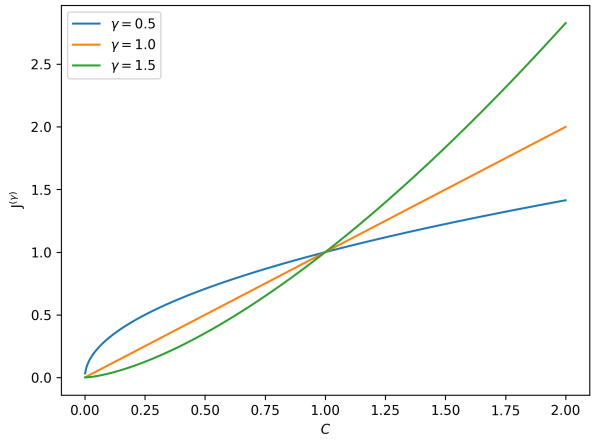

Figure 2.2: Maintenance cost $J^{(\gamma)}$ associated with a single edge as a function of its conductance C, for different constant values of the exponent γ.

and loop-favoring ($\gamma > 1$) regimes, while $\ell \in [0,1]$ sets the location of the transition within the flow range.

This formulation allows different topological tendencies to coexist within the same network as a function of the local flow. Unlike mechanisms based on temporal variability, stochastic forcing, or damage and repair [Corson, 2010, Katifori et al., 2010, Ronellenfitsch and Katifori, 2019], tree–loop coexistence here emerges in fully stationary conditions, under fixed forcing and steady flows [Giaccone et al., 2025].

For low flow rates, $\gamma(Q)$ remains close to unity, favoring distributed transport and loop formation. As the flow increases, $\gamma(Q)$ decreases below one, progressively promoting the concentration of transport into dominant paths.

In the following chapters, the cost functional (2.1), together with the maintenance models introduced here, is used to generate optimized transport networks through numerical minimization. optimization principle, and serve as analytically tractable reference structures to investigate scaling laws, wall shear stress distributions, and equivalent hydraulic descriptors.

2.3 Remarks on modeling closures

The relations (1.5) and (1.7) are employed here as algebraic closures to compare optimization outcomes under different hydraulic scalings. The numerical tests are performed on a stylized setup (regular grid, uniform sinks, and simplified fluid properties; see Table 4.1), for which most edges operate at relatively low Reynolds numbers.

As a consequence, the fully developed turbulent closure is applied outside its strict range of physical validity. In this context, the turbulent law predicts lower wall shear stresses τ_w than the laminar one. The two closures intersect only at much higher Reynolds numbers, as shown in the τ_w–Re comparison in Figure 2.3. The resulting configurations

should therefore be interpreted as model outcomes rather than as quantitative predictions for real pipe flows.

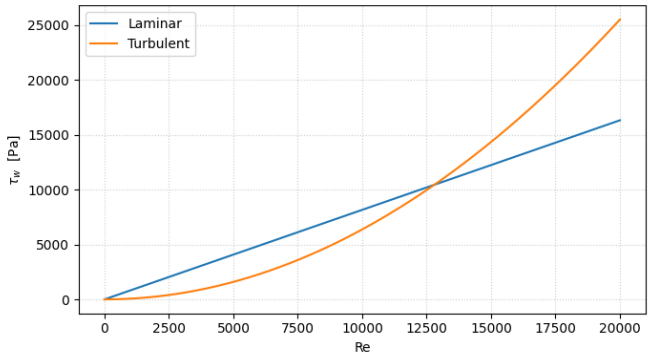

Figure 2.3: Comparison of wall shear stress τ_w versus Reynolds number Re for the laminar and fully developed turbulent closures.

Chapter 3

Numerical Methods and Experimental Design

3.1 Domain and forcing

The computational domain is defined as a regular square grid of size $n \times n$, consisting of $N = n^2$ nodes. Nodes are connected by directed edges linking nearest neighbors on the grid.

External forcing is prescribed through nodal source terms. A single source of total strength $s_0 > 0$ is placed at a designated inlet node (labelled 0 in all simulations, top–left in all figures). All remaining nodes act as identical sinks, each withdrawing an equal fraction of the injected flow,

$$s_i = -\frac{s_0}{N-1}, \qquad \forall i \neq 0, \tag{3.1}$$

so that global mass conservation is satisfied by construction. The pressure field is made unique by fixing the reference pressure at the inlet node, $P_0 = 0$.

This source–sink configuration represents a drainage-type transport problem, in which flow injected at a single inlet is distributed throughout the domain and removed uniformly. The forcing pattern is kept fixed across all numerical experiments, allowing differences in the resulting network architectures to be attributed solely to the hydraulic regime, the maintenance model, and the optimization dynamics.

3.2 Optimization Algorithm

Optimized transport networks are computed through an iterative relaxation algorithm that alternates between solving the flow problem for a fixed conductance field and updating the conductances according to the optimality conditions of the cost functional [Giaccone et al., 2025]. The procedure is fully deterministic: for a given initialization and set of parameters, it converges to the same stationary configuration.

At iteration t, the algorithm consists of the following steps:

1. **Initialization.** Once the maintenance model for γ is selected, initial conductances $C_{ij}^{(0)}$ are assigned on the admissible edge set by sampling from a uniform distribution,

$$C_{ij}^{(0)} \sim \mathcal{U}(0, c).$$

An example of the initial condition is shown in Fig. 3.1, where thicker edges correspond to larger conductances.

In the fully laminar and fully developed turbulent scenarios, all edges are assigned the corresponding regime for the entire simulation. In the mixed regime, all edges are initially classified as laminar, and the regime assignment is subsequently updated during the iteration.

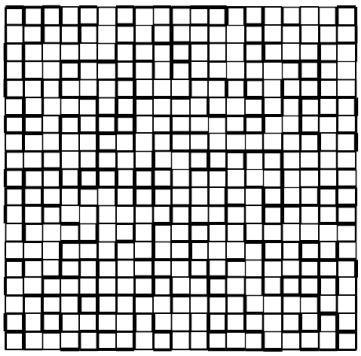

Figure 3.1: Example of initial conductances used in the relaxation algorithm; thicker lines indicate higher conductance values.

2. **Flow solve.** Given the current conductances $C^{(t)}$ and the corresponding regime assignment (i.e. the edgewise exponent α_{ij}), the nodal pressures $P^{(t)}$ are computed by enforcing mass conservation at each node, together with the constitutive law:

$$Q_{ij} = C_{ij} \left(\Delta P_{ij}\right)^{\alpha_{ij}}.$$

This step yields the flow field $Q^{(t)}$ consistent with the current network configuration.

For $\alpha_{ij} \neq 1$, the nodal mass-balance equations define a nonlinear system for the pressures, which can be written compactly as $F(P) = 0$. This system is solved using a Newton method. At iteration k of the Newton procedure, the linearized system

$$\mathbf{J}(P^{(k)})\, \delta P = -F(P^{(k)})$$

is solved, where $\mathbf{J} = \partial F / \partial P$ is the Jacobian matrix of the residuals. The pressures are updated using a damping factor:

$$P^{(k+1)} = P^{(k)} + \kappa\, \delta P.$$

The Newton iteration is terminated when the residual norm falls below a specified tolerance.

In the purely laminar case ($\alpha = 1$), the system of equations becomes linear and, therefore, the Newton method is not necessary. Instead, a standard linear solver is used to solve for the pressures.

3. **Conductance update.** For fixed flows $Q^{(t)}$, the cost functional is minimized locally with respect to each conductance $C_{ij} > 0$. Minimizing

$$\frac{Q_{ij}^{(1+\alpha_{ij})/\alpha_{ij}}}{C_{ij}^{1/\alpha_{ij}}} + b\, C_{ij}^{\gamma_{ij}}$$

with respect to C_{ij} yields the closed-form update

$$C_{ij}^{*} = \Big(\frac{1}{b\,\gamma_{ij}}\Big)^{\frac{\alpha_{ij}}{\alpha_{ij}\gamma_{ij}+1}} \big|Q_{ij}^{(t)}\big|^{\frac{\alpha_{ij}+1}{\alpha_{ij}\gamma_{ij}+1}}. \tag{3.2}$$

The updated conductances are then set as $C^{(t+1)} \leftarrow C^{*}$.

4. **Regime update (mixed case only).** In the mixed laminar–turbulent configuration, local Reynolds numbers Re_{ij} are recomputed and the regime exponent α_{ij} is updated edgewise according to the threshold criterion:

$$Re_{ij} \le Re_c \;\Rightarrow\; \text{laminar}, \qquad Re_{ij} > Re_c \;\Rightarrow\; \text{fully developed turbulent}.$$

5. **Convergence test.** The iteration steps (2, 3, and 4) are repeated until convergence. The iteration is stopped when the maximum relative variation of the conductances between two successive iterations falls below a prescribed tolerance.

With this procedure, the optimization algorithm converges to a local minimum of the cost functional, where the conductances and flow distribution are adjusted to balance hydraulic efficiency and maintenance costs.

3.3 Post-processing metrics

The post-processing analysis relies on the local hydraulic fields defined in Section 1.5, namely the edgewise flow rate Q_{ij}, Reynolds number Re_{ij}, wall shear stress $\tau_{w,ij}$, and equivalent radius r_{ij}. These quantities are evaluated on the network configuration at each iteration and on the final converged state, and are used to characterize both the local and global properties of the optimized networks.

Flow rate. The distribution of the flow rate Q_{ij} across the edges provides a direct measure of how transport is organized within the network. Its statistics are used to assess the degree of flow heterogeneity and the emergence of dominant transport pathways under different maintenance models and hydraulic regimes.

Reynolds number. The Reynolds number Re_{ij} is employed both as a diagnostic quantity and, in mixed-regime configurations, as a classifier of the local flow regime. Its distribution quantifies the extent to which laminar and turbulent branches coexist within the same network and how this balance evolves with demand.

Wall shear stress. The wall shear stress $\tau_{w,ij}$ characterizes the mechanical load exerted by the flow on conduit walls. Its spatial distribution and statistics provide insight into the heterogeneity of local stresses and into the signatures of different hydraulic closures, particularly in mixed laminar–turbulent configurations.

Equivalent radius. The equivalent hydraulic radius r_{ij}, inferred from the conductance of each edge, serves as a geometric descriptor of the network. Its distribution reflects how material is allocated across the network and allows a direct comparison between optimized transport networks and prescribed geometries, such as deterministic trees.

3.3.1 Statistical analysis of distributions

For each of the quantities mentioned above, we compute their distribution across the edges of the optimized networks, considering different realizations. The following statistical metrics are employed to analyze the distributions:

- **Mean**: the average value of the distribution, which provides a measure of the central tendency.
- **Coefficient of variation**: a relative measure of variability, defined as the ratio of the standard deviation to the mean, which quantifies the dispersion of the distribution.
- **Cumulative distribution function (CDF)**: a function that shows the cumulative probability of the variable being less than or equal to a certain value. It provides a comprehensive view of the distribution.
- **Scaling exponent fitting**: For the tails of the distributions, a power-law model is fitted to determine the scaling exponents.

Cost function. In addition to the statistical analysis of flow-related quantities, we also take into account the evolution of the cost function J throughout the optimization process. Tracking the progression of J provides valuable insight into how the network is balancing hydraulic performance with structural investment, and converging to the (local) optimum.

These metrics allow for a detailed characterization of the network's behavior under various hydraulic conditions and maintenance models. They provide insight into how the system behaves at both the global and local levels.

The detailed analysis of these diagnostic metrics, based on simulation outcomes, will be provided in Chapter 4.

3.4 Demand sweep protocols

In order to trigger and quantify laminar–turbulent transitions in mixed-regime configurations, we also perform a sweep of the total injected demand s_0 while keeping the source–sink pattern and the physical parameters fixed. The sweep is designed to explore how the regime assignment changes as the overall throughput increases, and how this transition is reflected in network-level observables. In the fully laminar and fully turbulent scenarios the regime assignment is uniform by construction, so the demand sweep is only meaningful in the mixed configuration. We will limit this analysis to the case of $\gamma = \frac{1}{2}$.

3.4.1 Setup of the sweep

We consider the drainage forcing introduced in Section 3.2: a single source of total strength $s_0 > 0$ is imposed at the inlet node 0, balanced by uniform sinks at all other nodes,

$$s_i = -\frac{s_0}{N-1}, \qquad i \neq 0.$$

For each value of s_0 in the sweep, the flow problem is solved on the network subject to the usual constraints Eq. (1.2) and Eq. (1.3). The regime exponent is assigned edgewise using a Reynolds threshold:

$$\alpha_{ij} = \begin{cases} 1, & Re_{ij} \leq Re_c \quad \text{(laminar)}, \\ \frac{1}{2}, & Re_{ij} > Re_c \quad \text{(turbulent, rough walls)}. \end{cases}$$

Here Re_c is a prescribed modeling threshold whose role is to enable coexistence of laminar and turbulent branches over the range of demands considered. The Reynolds number is computed from the local flow rate and the equivalent diameter, consistently with Section 1.5.

3.4.2 Two sweep protocols: re-optimized vs rigid sweep

We compare two protocols that differ in whether the network geometry is allowed to adapt as demand varies.

Re-optimized sweep. For each prescribed s_0, the network is *fully re-optimized* at that demand level. Operationally, starting from an initial conductance field, we iterate the relaxation algorithm of Section 3.2 until convergence: (i) solve the (possibly nonlinear) mass-balance system for nodal pressures and edge flows, (ii) update conductances using the local optimality condition of the cost functional, and (iii) reclassify each edge as laminar/turbulent according to Re_c. We repeat until convergence or short periodicity is reached. On the converged snapshot we compute post-processing observables.

This protocol represents *co-adaptation*: conductances (and hence equivalent radii) and regime labels are allowed to reorganize together as the global throughput increases.

Rigid sweep (fixed radii). In the rigid protocol, the geometric degrees of freedom are frozen. We first perform a single laminar-only optimization at a reference demand (used as baseline), obtaining a reference conductance/radius field $\{C_{ij}\}$ (equivalently $\{r_{ij}\}$). Then, during the sweep over s_0, we keep C_{ij} and r_{ij} fixed, and recompute only pressures and flows for each new demand. In the mixed case, edges are still re-labeled as laminar/turbulent through the Reynolds criterion, but without any further conductance update.

This protocol isolates the effect of changing throughput on a fixed architecture, and can be interpreted as a hydraulic sweep rather than a morphological one.

3.4.3 Turbulent fraction

Let $\mathcal{E}$ denote the active edge set at the converged snapshot and let $\mathcal{E}_{\text{turb}} \subseteq \mathcal{E}$ be those classified as turbulent. We define the turbulent fraction as

$$\phi_{\text{turb}} \;=\; \frac{|\mathcal{E}_{\text{turb}}|}{|\mathcal{E}|} \in [0,1]. \tag{3.3}$$

As s_0 increases (equivalently, as $-s_i$ increases), larger portions of the network cross the critical Reynolds threshold and ϕ_{turb} typically grows from 0 toward 1.

Normalization by a characteristic demand. To compare sweeps across different grid sizes n, we report the turbulent fraction as a function of the normalized sink demand

$$\tilde{s}_i \;=\; \frac{s_i}{s^\star}, \qquad s^\star \;=\; \min\{-s_i \;:\; \phi_{\text{turb}}(s_i) \geq \phi_{\text{sat}}\}, \tag{3.4}$$

where ϕ_{sat} is a prescribed saturation level. With this definition, $\tilde{s}_i \approx 1$ marks the onset of near-full turbulence in the active set, and the transition curves $\phi_{\text{turb}}(\tilde{s}_i)$ can be compared across network sizes on a common axis.

3.4.4 Equivalent resistance

To quantify network-level hydraulic performance, we introduce an equivalent resistance tailored to drainage configurations. Let the total mechanical power dissipated at the converged snapshot be

$$J^{(D)} \;=\; \sum_{(i,j)\in\mathcal{E}} Q_{ij}\,\Delta P_{ij}. \tag{3.5}$$

We define the equivalent pressure drop ΔP_{eq} through the identity

$$J^{(D)} \;=\; s_0\,\Delta P_{\text{eq}}, \tag{3.6}$$

and the equivalent resistance as

$$R_{\text{eq}} \;=\; \frac{\Delta P_{\text{eq}}}{s_0} \;=\; \frac{J^{(D)}}{s_0^2}. \tag{3.7}$$

This definition treats the entire network as an effective two-terminal device relating the injected flow s_0 to an equivalent head loss, while remaining well-defined in the presence

of distributed sinks. The equivalent pressure drop ΔP_{eq} is defined in a purely operational sense: it is the pressure drop that, if applied to a hypothetical single inlet–outlet device carrying the same total flow s_0, would dissipate the same total mechanical power as the network.

For each grid size and each sweep protocol, the procedure is repeated over multiple random initializations (seeds) of the conductances in the optimization runs. At each demand level we will compute ϕ_{turb} and R_{eq} on the converged snapshot, and report the mean curves together with uncertainty bands (95% confidence intervals across seeds).

Chapter 4

Numerical Results on OTNs

This chapter presents numerical results for *optimized transport networks* (OTNs) within the graph-based hydraulic framework introduced in Chapter 1, under the hypotheses of Chapter 2.

A central goal of this thesis is to isolate how *hydraulic physics* and *maintenance modeling* shape optimal network structure and statistics. On the hydraulic side, we compare the three regime assignments introduced in Section 1.4: fully laminar ($\alpha = 1$), fully rough turbulent ($\alpha = \frac{1}{2}$), and mixed laminar–turbulent configurations where the exponent α_{ij} switches edgewise according to a Reynolds threshold Re_c. On the maintenance side, we contrast a concave, constant maintenance exponent $\gamma = \frac{1}{2}$ with a flow-dependent model $\gamma(Q)$ (Eq. (2.5)), which locally modulates the cost of sustaining conductance and promotes departures from strictly tree-like architectures.

Throughout the chapter we monitor the diagnostics described in Section 1.5. The baseline parameters used throughout this chapter are summarized in Table 4.1.

The chapter is organized as follows. Section 4.1 documents convergence of the optimization procedure through objective and dissipation traces, together with the evolution of representative hydraulic diagnostics. Section 4.2 then compares the resulting optimal topologies and spatial fields (flows, Re, and τ_w) across regimes and maintenance models. Section 4.3 quantifies statistical regularities by reporting global distributions of Q, Re, τ_w, and r, and by fitting scaling exponents from pooled simulations.

Finally, Section 4.4 investigates how mixed-regime networks transition from predominantly laminar to predominantly turbulent behavior as the overall throughput is increased. These demand-sweep experiments are performed with dedicated parameter sets (reported in the corresponding tables).

Group	Quantity	Symbol	Value
Geometry	Grid size	n	20 nodes per side
	Number of nodes	N	400
	Edge length	L_{ij}	1.0 m
Supply/demand	Source at node 0	s_0	399
	Sinks ($i \neq 0$)	s_i	-1
Fluid	Gravity	g	9.81 m s^{-2}
	Kinematic viscosity	ν	1.0 m^2 s^{-1}
	Dynamic viscosity	μ	1.0 Pa s
	Specific weight	γ_f	1.0 N m^{-3}
Friction	Friction factor	f	$5 \cdot 10^{-3}$
Mixed regime	Threshold	Re_c	7.0
Cost function	Metabolic factor	b	1.0
	Constant maintenance exp.	γ	0.5
Flow-dependent γ	Amplitude	δ	1.0
	Location	ℓ	0.01
Optimization	Newton damping	κ	0.5
	Tolerance	ε	10^{-6}

Table 4.1: Model, regime, and optimization parameters used in the baseline OTN simulations.

4.1 Convergence and optimization traces

To assess the stability of the relaxation scheme and provide a compact view of the optimization dynamics, we monitor both the objective function and a set of hydraulic diagnostics across iterations for representative runs, one for each regime and maintenance combination. Figure 4.1 reports the evolution of the total cost J together with the purely hydraulic dissipation term $J^{(D)}$. In all regimes, the two curves decrease in a strongly correlated fashion and rapidly approach a plateau, indicating that the conductance updates consistently reduce dissipation while simultaneously improving the full objective.

At convergence, the laminar simulations reach $J \approx 4 \cdot 10^3$ for both maintenance models, the turbulent runs settle around $J \approx 3 \cdot 10^3$, and the mixed case lies in between. The fact that the fully turbulent setting yields the smallest J is counterintuitive from a physical standpoint, but it is a direct consequence of the parameter choice in this test: the resulting Reynolds numbers remain mostly in a low-Re range where the fully-developed turbulent closure is not expected to be valid, so imposing the turbulent exponent effectively underestimates the hydraulic penalty and lowers the computed objective.

Beyond the objective traces, Fig. 4.2 summarizes the evolution of the Reynolds statistics over the active edge set. After an initial transient, the mean Reynolds number rapidly

converges to a stationary value, indicating that the global flow regime of the network stabilizes early in the optimization. In parallel, the coefficient of variation decreases and eventually plateaus, signaling the progressive homogenization of relative fluctuations across edges and the attainment of a statistically steady hydraulic configuration.

Figure 4.3 shows analogous trends for the wall shear stress τ_w. In the mixed regime, small oscillations can persist longer than in the purely laminar/turbulent cases; we attribute this to edges hovering near the threshold Re_c and being reclassified across iterations, which introduces a mild "switching" noise in the effective constitutive law.

Overall, the joint stabilization of J, Re, and τ_w supports the use of these convergence traces as practical diagnostics for terminating the relaxation procedure.

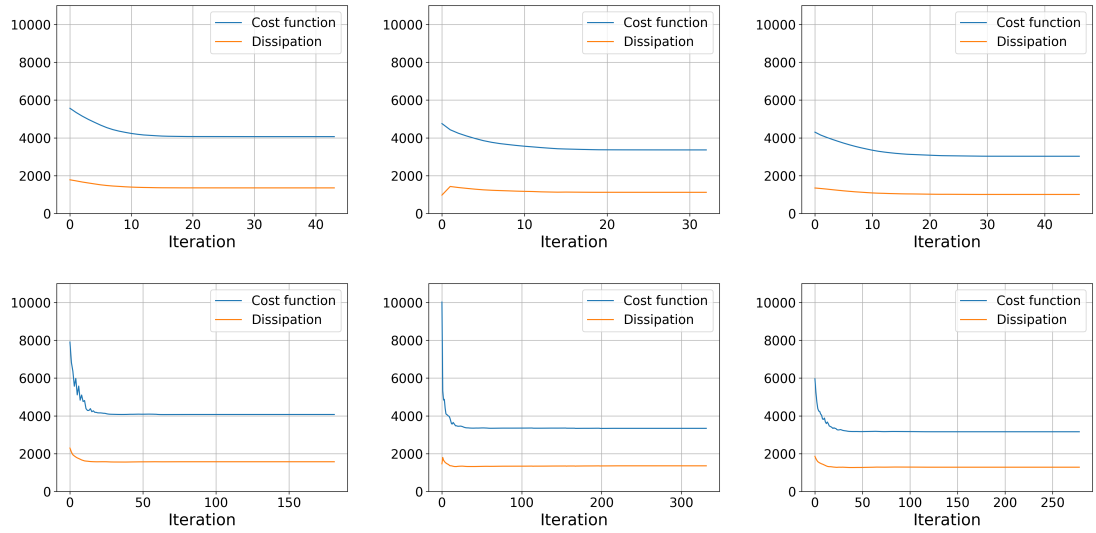

Figure 4.1: Cost function and dissipation over optimization iterations for the laminar (left), mixed laminar–turbulent (center), and turbulent (right) cases, with $\gamma = \frac{1}{2}$ (top row) and $\gamma = \gamma(Q)$ (bottom row).

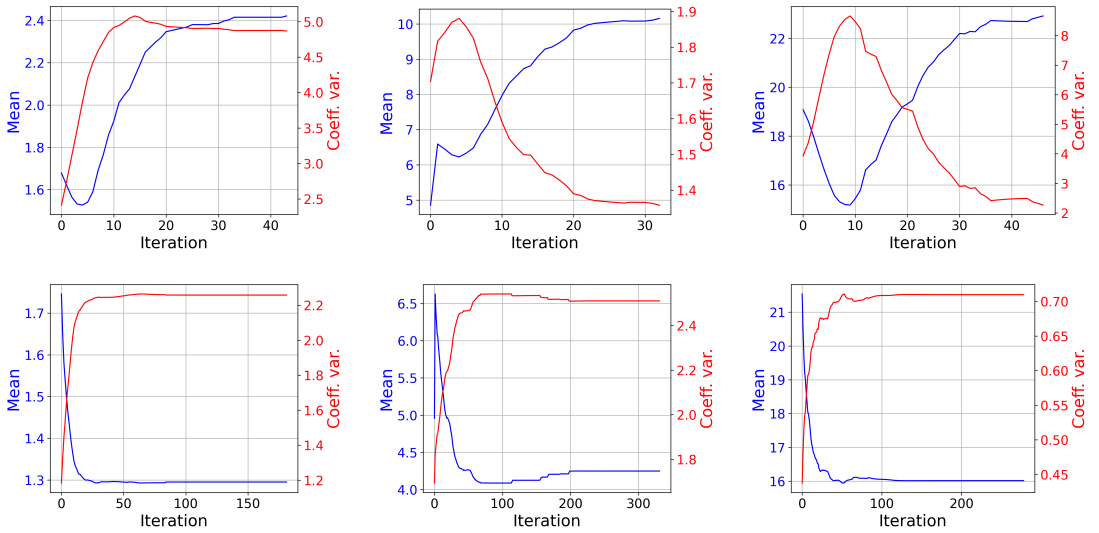

Figure 4.2: Mean and coefficient of variation of Re over optimization iterations for the laminar (left), mixed laminar–turbulent (center), and turbulent (right) cases, with $\gamma = \frac{1}{2}$ (top row) and $\gamma = \gamma(Q)$ (bottom row).

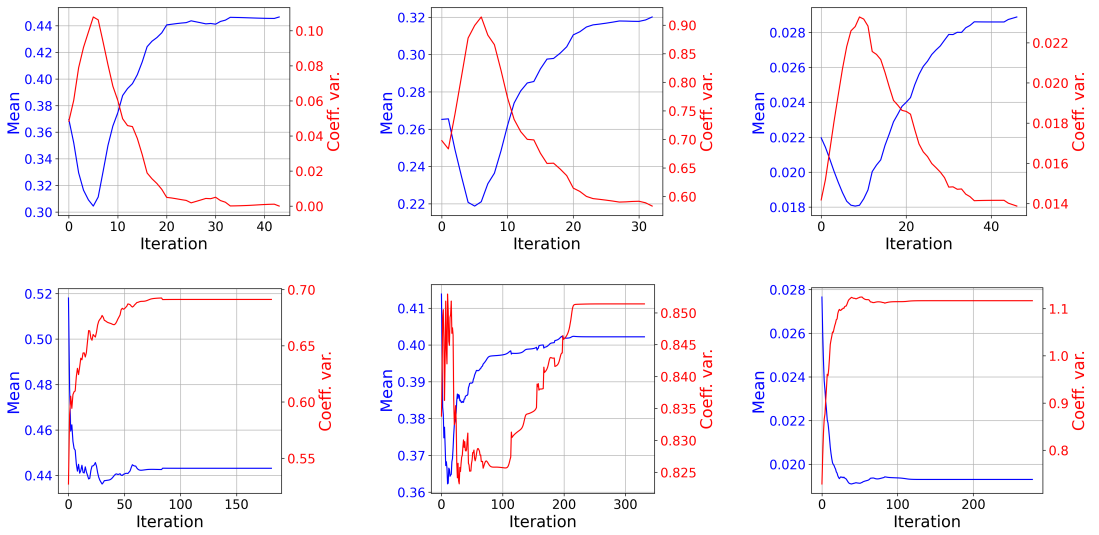

Figure 4.3: Mean and coefficient of variation of τ_w over optimization iterations for the laminar (left), mixed laminar–turbulent (center), and turbulent (right) cases, with $\gamma = \frac{1}{2}$ (top row) and $\gamma = \gamma(Q)$ (bottom row).

We now turn from convergence properties to structural and statistical features.

4.2 Topology and edge fields

We begin by comparing the optimal network topologies obtained under the three hydraulic regimes and the two maintenance models. Figure 4.4 displays the converged networks, where edge thickness is proportional to the carried flow Q_{ij} and thus highlights the dominant transport paths.

For the constant maintenance exponent $\gamma = \frac{1}{2}$, the optimal solution is strictly tree-like in all three hydraulic scenarios (laminar, mixed, and turbulent), in agreement with the concavity of the maintenance cost. When the flow-dependent maintenance model $\gamma(Q)$ is adopted, the solutions remain dominated by a single main backbone but develop small peripheral loops, typically associated with low-flow regions. Despite these local differences, the three hydraulic scenarios yield networks that are topologically very similar within each maintenance model, indicating that, at this level, the large-scale organization is primarily controlled by maintenance rather than by the constitutive flow exponent.

Figure 4.5 shows the same optimal networks with edges colored by the local Reynolds number. As expected, Re_{ij} strongly correlates with the magnitude of the flow and reaches its largest values along the main transport tree connecting the inlet to the bulk of the sinks. In the mixed laminar–turbulent regime, a sharp color contrast marks the interface between laminar and turbulent edges, directly reflecting the edgewise switch of the constitutive exponent at the threshold $Re_c = 7$. This value should be interpreted as a modeling parameter rather than a physical transition: it is chosen pragmatically to allow laminar and turbulent segments to coexist within the same network for the baseline parameter set.

Finally, Fig. 4.6 reports the optimal networks with edges colored by the wall shear stress τ_w. In contrast to the flow rate and the Reynolds number, the dominant transport paths are associated with *smaller* values of τ_w, while larger wall shear stresses are observed on thinner, downstream branches. Thus, the spatial organization of τ_w is effectively inverted with respect to that of Q_{ij} and Re_{ij}.

For the present parameter choices, edges classified as turbulent typically exhibit lower values of τ_w than laminar ones. This behavior should not be interpreted as a physical prediction: as discussed in Section 2.3, the laminar and fully developed turbulent closures intersect only at Reynolds numbers far above those realized in these simulations (see Fig. 2.3). In the low-Re range explored here, applying the turbulent closure effectively reduces the estimated wall shear stress, explaining the systematically smaller τ_w observed along the dominant paths.

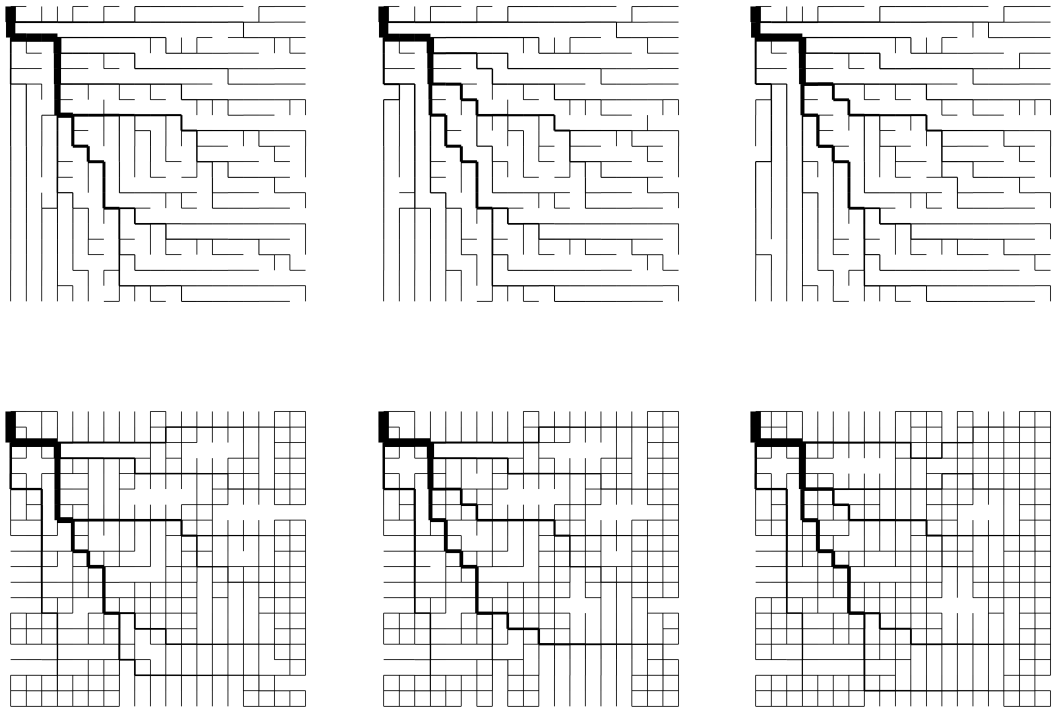

Figure 4.4: Optimal network configurations for the laminar (left), mixed laminar–turbulent (center), and turbulent (right) cases, with $\gamma = \frac{1}{2}$ (top row) and $\gamma = \gamma(Q)$ (bottom row).

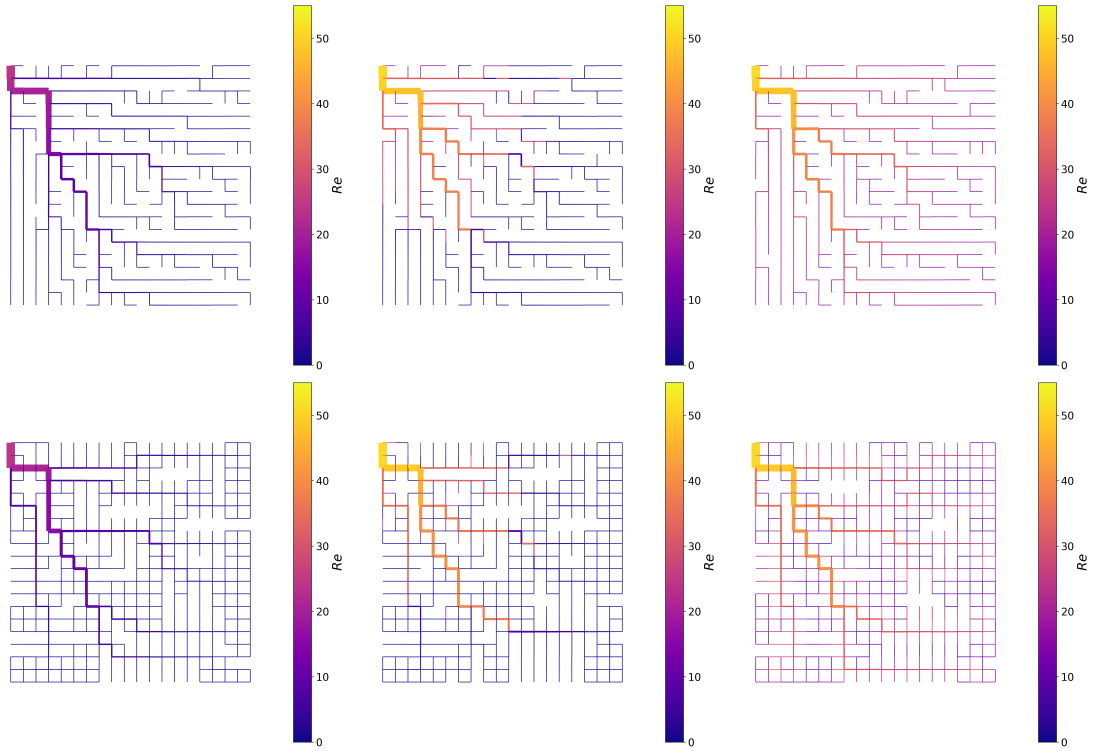

Figure 4.5: Optimal network with edges colored by Re for the laminar (left), mixed laminar–turbulent (center), and turbulent (right) cases, with $\gamma = \frac{1}{2}$ (top row) and $\gamma = \gamma(Q)$ (bottom row). $Re_c = 7$.

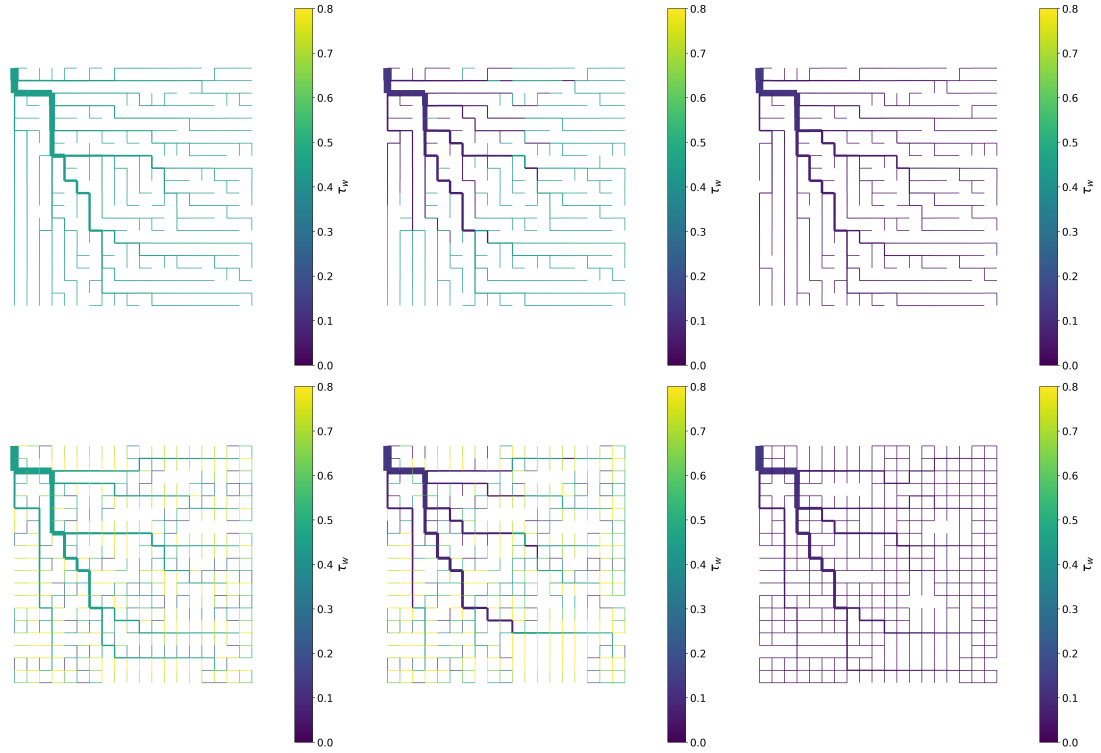

Figure 4.6: Optimal network with edges colored by τ_w for the laminar (left), mixed laminar–turbulent (center), and turbulent (right) cases, with $\gamma = \frac{1}{2}$ (top row) and $\gamma = \gamma(Q)$ (bottom row).

4.3 Statistical distributions

To assess the statistical robustness of the optimal solutions, we analyze the edgewise distributions of flow Q, Reynolds number Re, wall shear stress τ_w and equivalent radius r. All distributions are obtained by pooling data from 10 independent simulations with different random initializations of the conductance field. For each hydraulic regime and maintenance model, we report histograms (top rows) together with the corresponding cumulative distribution functions (bottom rows), allowing both the bulk behavior and the tail structure to be examined. Table 4.2 summarizes the scaling exponents extracted from the global distributions.

Flow Q. Across both maintenance models ($\gamma = \frac{1}{2}$, Fig. 4.7, and $\gamma = \gamma(Q)$, Figs. 4.8), the flow distributions are strongly right-skewed, with a large fraction of edges carrying very small flow. Under constant maintenance ($\gamma = \frac{1}{2}$, the tails display a clear power-law–like behavior on log–log axes, which is well captured by the fitted interpolations. Remarkably, the three hydraulic scenarios (laminar, mixed, and turbulent) yield nearly indistinguishable Q statistics, as confirmed by the close agreement of the fitted exponents reported in Table 4.2. This insensitivity reflects the fact that the large-scale flow organization is primarily controlled by the maintenance term, rather than by the precise constitutive exponent.

Reynolds number Re. In the laminar and mixed configurations, the Reynolds number distributions closely mirror those of the flow, consistent with the monotonic dependence $Re \propto Q$ for fixed geometry. Most edges operate at low Reynolds numbers, with a rapidly decaying tail toward larger values. In contrast, the fully turbulent scenario exhibits a broader distribution, with a larger weight at intermediate Re and a relative scarcity of very small values. For $\gamma = \frac{1}{2}$ the fitted slopes are in good agreement with the visual trends observed in the cumulative distributions (Figs. 4.9 and 4.10).

Wall shear stress τ_w. The distributions of wall shear stress show the most pronounced differences across hydraulic regimes (Figs. 4.11 and 4.12). For constant maintenance, the laminar case spans a very narrow range of τ_w, reflecting the nearly linear pressure–flow relation and the homogeneous scaling of stresses. The fully turbulent case, by contrast, extends over a much wider interval. The mixed regime displays a clearly bimodal structure, with a narrow laminar peak coexisting with a broader turbulent component, directly reflecting the edgewise regime assignment. When the flow-dependent maintenance model $\gamma(Q)$ is used, all three scenarios become more broadly distributed, indicating increased heterogeneity in local loads induced by the adaptive maintenance rule.

Equivalent radius r. The equivalent radii span several orders of magnitude in all configurations, consistent with the strong hierarchy of flows in the optimized networks. Differences across hydraulic regimes are comparatively modest, although the fully turbulent scenario exhibits a slight skew toward smaller radii (Figs. 4.13 and 4.14).

Table 4.2 collects the scaling exponents obtained from power-law fits of the global distributions, providing a compact quantitative comparison across hydraulic regimes and maintenance models.

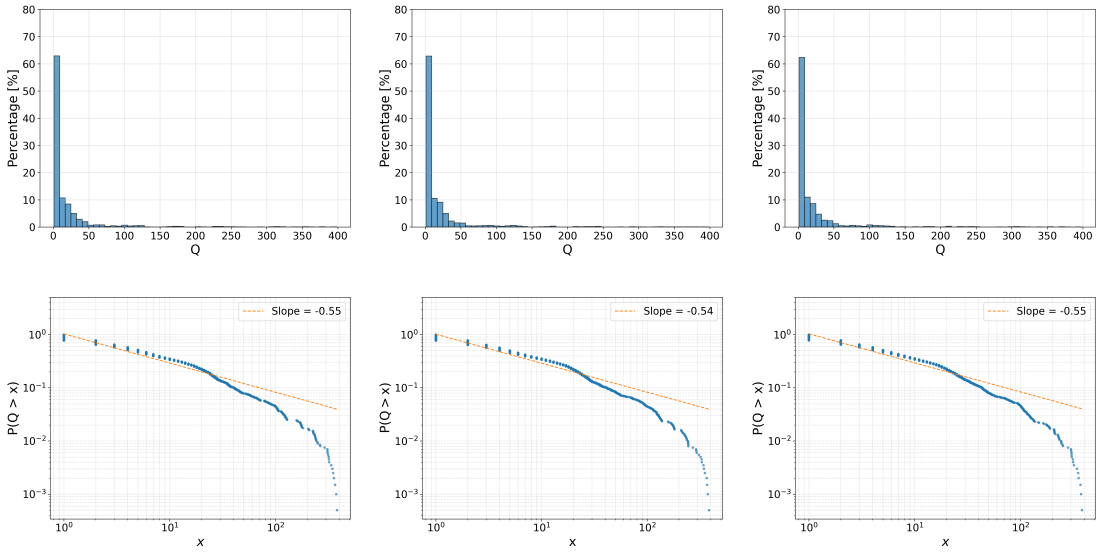

Figure 4.7: Q distributions for the laminar (left), mixed laminar–turbulent (center), and turbulent (right) cases, with $\gamma = \frac{1}{2}$. The distributions are obtained from statistics over 10 independent simulations.

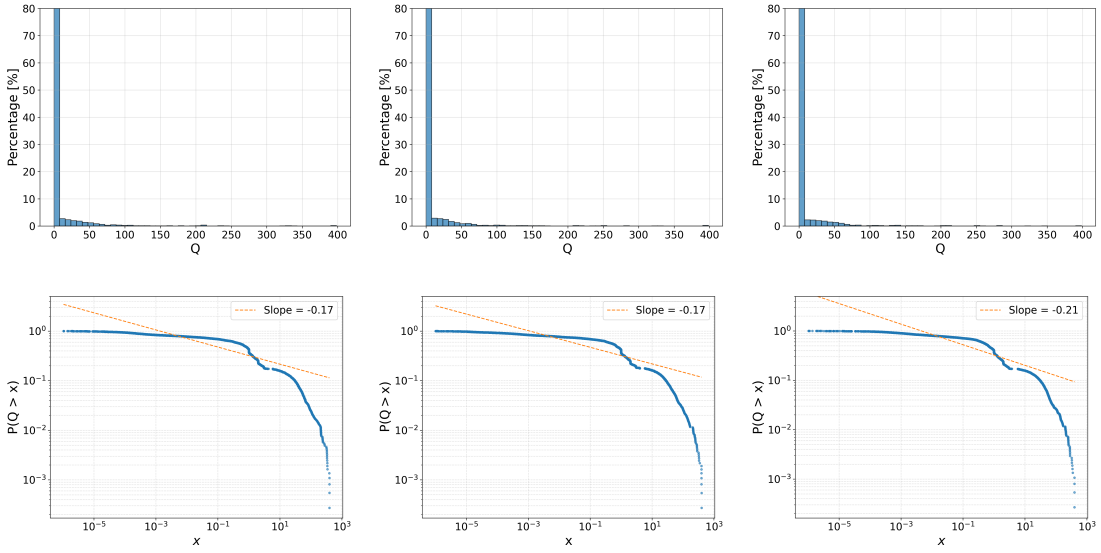

Figure 4.8: Q distributions for the laminar (left), mixed laminar–turbulent (center), and turbulent (right) cases, with $\gamma = \gamma(Q)$. The distributions are obtained from statistics over 10 independent simulations.

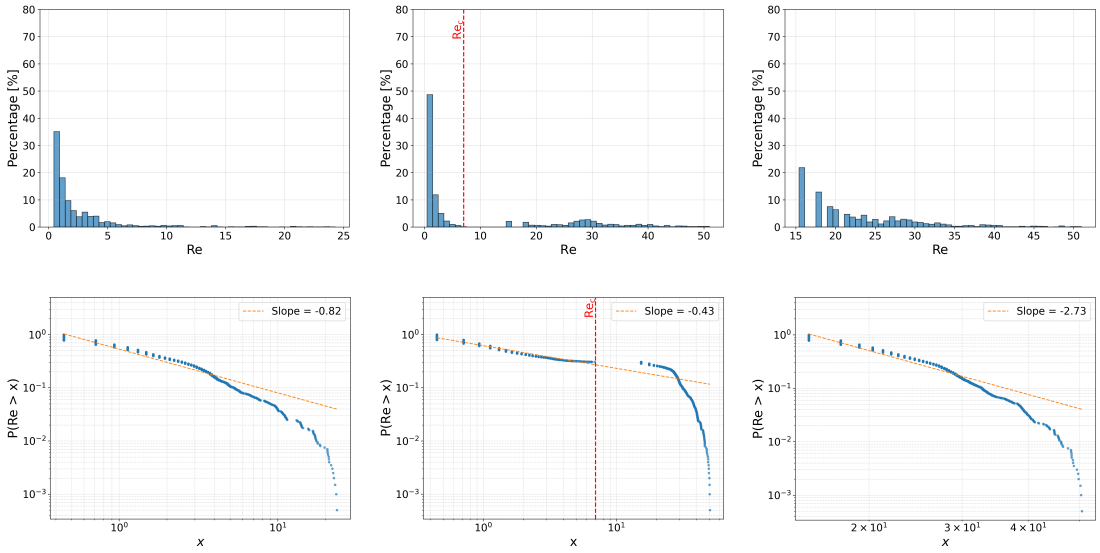

Figure 4.9: Re distributions for the laminar (left), mixed laminar–turbulent (center), and turbulent (right) cases, with $\gamma = \frac{1}{2}$. $Re_c = 7$. The distributions are obtained from statistics over 10 independent simulations.

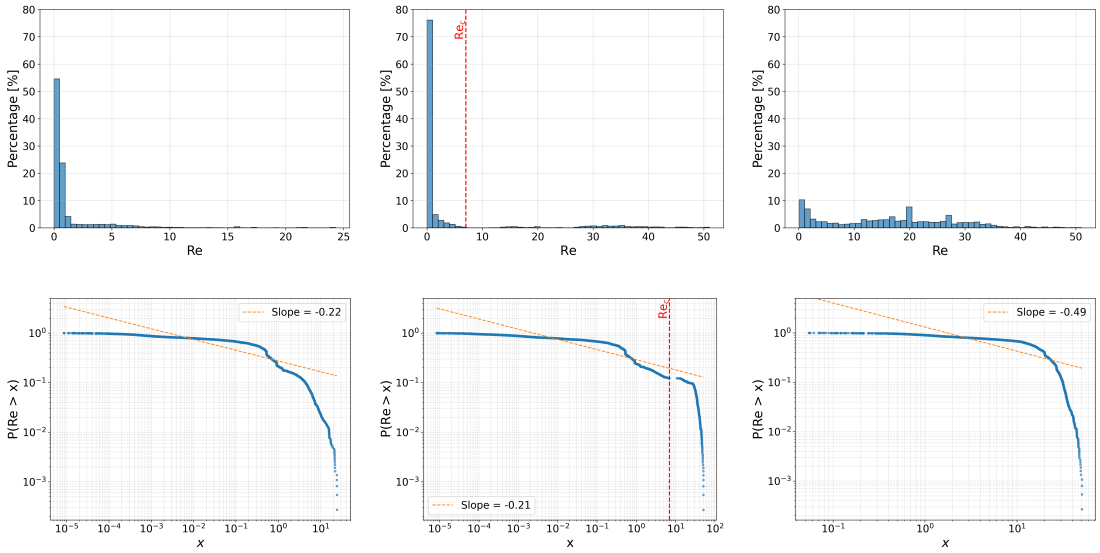

Figure 4.10: Re distributions for the laminar (left), mixed laminar–turbulent (center), and turbulent (right) cases, with $\gamma = \gamma(Q)$. The distributions are obtained from statistics over 10 independent simulations.

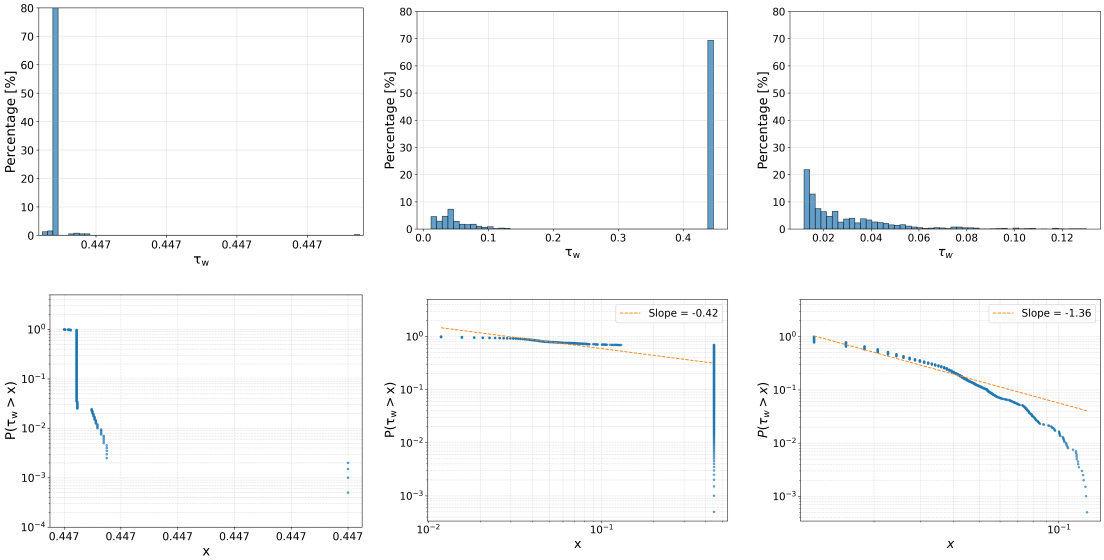

Figure 4.11: τ_w distributions for the laminar (left), mixed laminar–turbulent (center), and turbulent (right) cases, with $\gamma = \frac{1}{2}$. The distributions are obtained from statistics over 10 independent simulations.

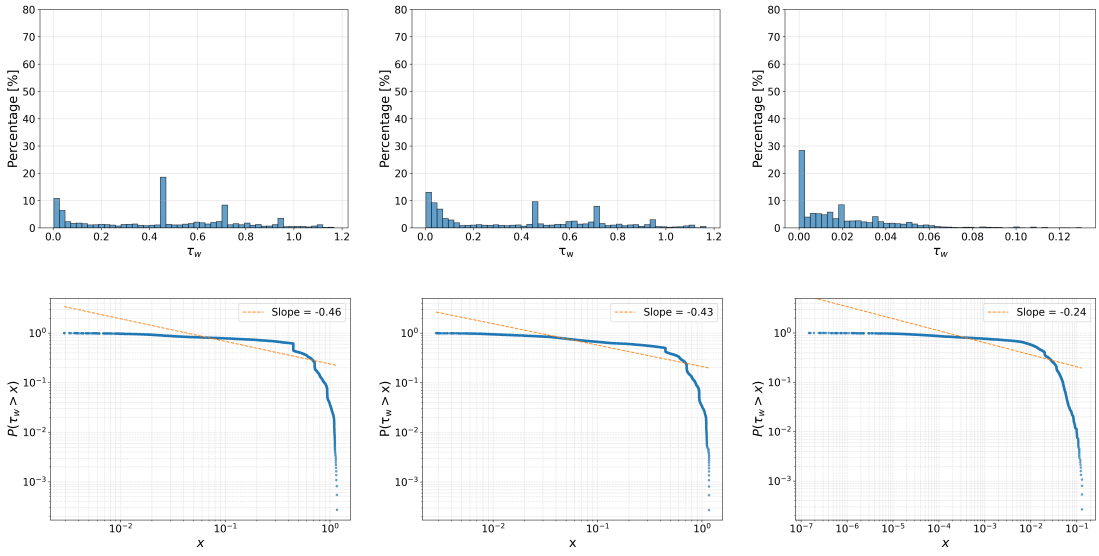

Figure 4.12: τ_w distributions for the laminar (left), mixed laminar–turbulent (center), and turbulent (right) cases, with $\gamma = \gamma(Q)$. The distributions are obtained from statistics over 10 independent simulations.

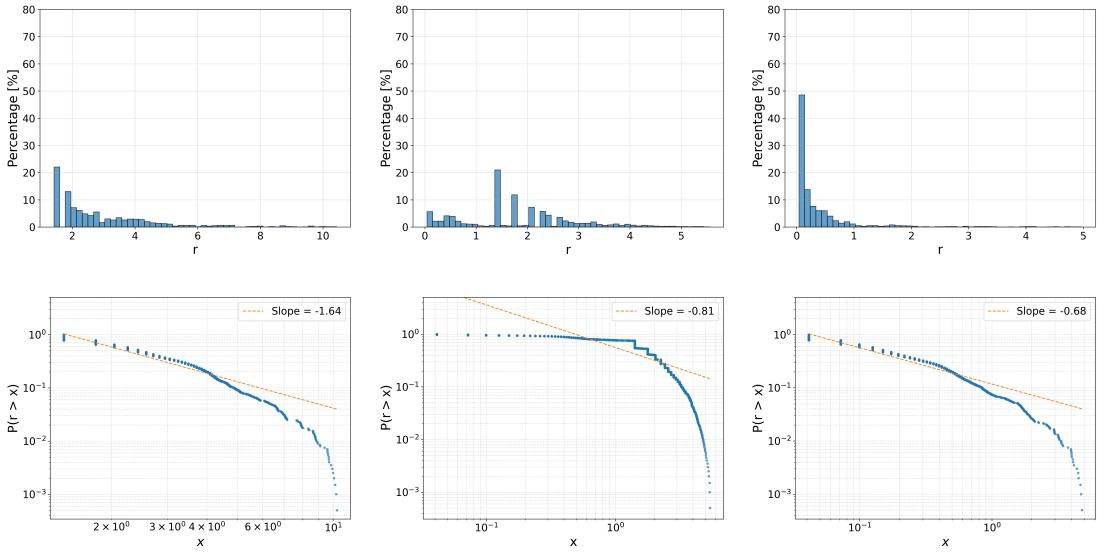

Figure 4.13: r distributions for the laminar (left), mixed laminar–turbulent (center), and turbulent (right) cases, with $\gamma = \frac{1}{2}$. The distributions are obtained from statistics over 10 independent simulations.

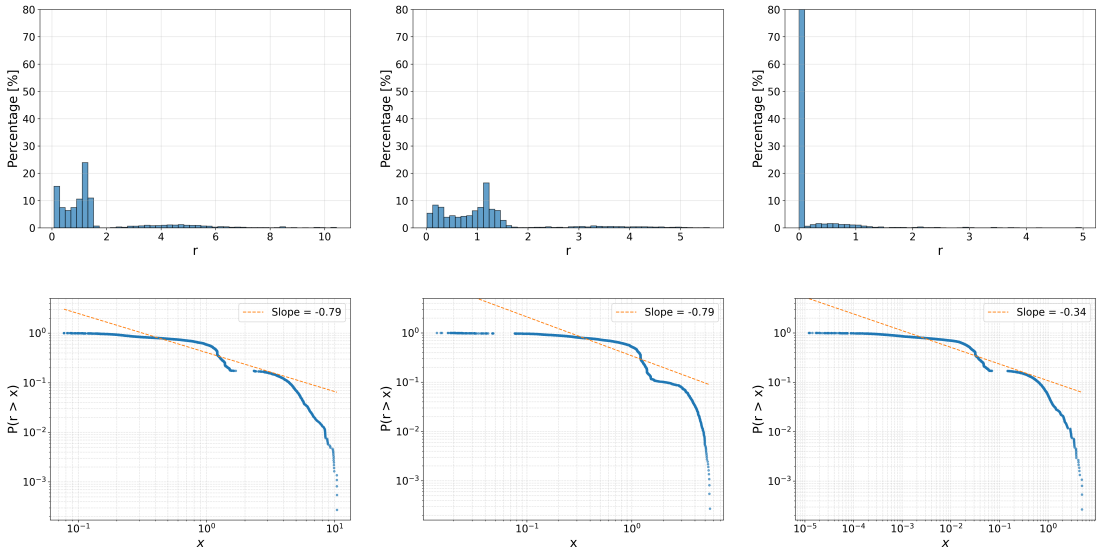

Figure 4.14: r distributions for the laminar (left), mixed laminar–turbulent (center), and turbulent (right) cases, with $\gamma = \gamma(Q)$. The distributions are obtained from statistics over 10 independent simulations.

	$\gamma = 1/2$				$\gamma = \gamma(Q)$			
	Q	Re	τ_w	r	Q	Re	τ_w	r
laminar	0.55	0.82	–	1.64	0.17	0.22	0.46	0.79
mixed	0.54	0.43	0.42	0.81	0.17	0.21	0.43	0.79
turbulent	0.55	2.73	1.36	0.68	0.21	0.49	0.24	0.34

Table 4.2: Scaling exponents of the global distributions of Q, Re, τ_w, and r for optimal networks with $\gamma = \frac{1}{2}$ and $\gamma = \gamma(Q)$.

4.4 Laminar–turbulent transition under increasing demand

We now present the results of the demand sweep experiments introduced in Section 3.4. In the following, we focus on the evolution of the turbulent fraction ϕ_{turb} and of the equivalent resistance R_{eq} as functions of the normalized demand $\tilde{s}_i$, and compare the outcomes of the re-optimized and rigid sweep protocols. All definitions and numerical procedures are as described in Section 3.4.

4.4.1 Re-optimized sweep

Figure 4.15 illustrates representative network snapshots at increasing demand for the re-optimized sweep. Turbulent edges consistently appear first on the largest-radius branches close to the source, where both flow rates and Reynolds numbers are maximal. As the total demand increases, turbulent segments progressively extend toward smaller downstream branches, eventually spanning the entire edges set.

The corresponding evolution of the turbulent fraction is shown in Fig. 4.16. For all grid sizes considered, ϕ_{turb} increases smoothly from zero to unity as $\tilde{s}_i$ grows. When plotted against the normalized demand, the transition curves collapse well across different system sizes.

The behavior of the equivalent resistance R_{eq} is reported in Fig. 4.17. Unlike the turbulent fraction, $R_{\text{eq}}(\tilde{s}_i)$ exhibits a non-monotonic dependence on demand.

Group	**Quantity**	**Symbol**	**Value**
Geometry	Edge length	L_{ij}	1.0 m
Fluid	Gravity	g	9.81 $\mathrm{m\,s^{-2}}$
	Kinematic viscosity	ν	$1.0{\cdot}10^{-3}$ $\mathrm{m^2\,s^{-1}}$
	Dynamic viscosity	μ	1.0 Pa s
	Density	ρ	$\mu/\nu = 10^3$ $\mathrm{kg\,m^{-3}}$
	Specific weight	γ_f	$g\,\rho = 9.81{\cdot}10^3$ $\mathrm{N\,m^{-3}}$
Friction	Turbulent factor	f	$5{\cdot}10^{-3}$
Mixed regime	Reynolds threshold	Re_c	4000
	Saturation threshold	ϕ_{sat}	0.99
Cost function	Metabolic factor	b	1.0
	Maintenance exponent (fixed)	γ	0.5

Table 4.3: Model, regime, and optimization parameters used in the mixed laminar/turbulent sweep.

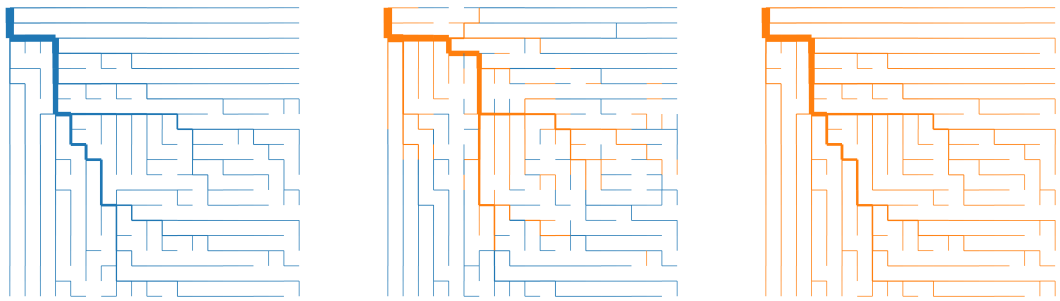

(a) Small s_0. (b) Medium s_0. (c) Large s_0.

Figure 4.15: Active edges colored by flow regime, for the re-optimized sweep: laminar edges ($\alpha = 1$) are shown in blue, while turbulent edges ($\alpha = 0.5$) are shown in orange. The spatial progression of turbulence with increasing demand highlights its hierarchical onset.

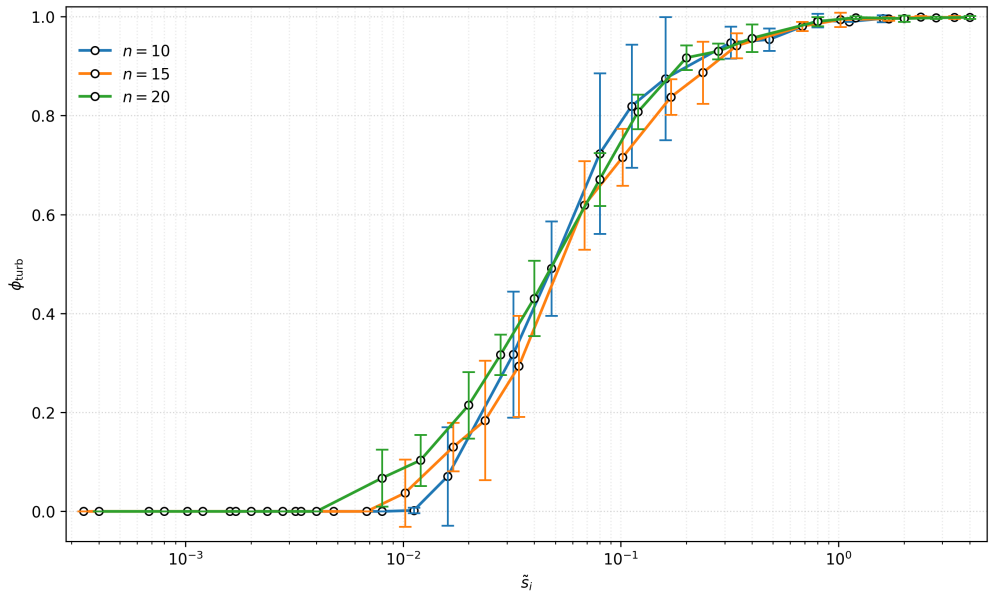

Figure 4.16: Turbulent fraction ϕ_{turb} versus normalized sink $\tilde{s}_i$ for multiple grid sizes n.

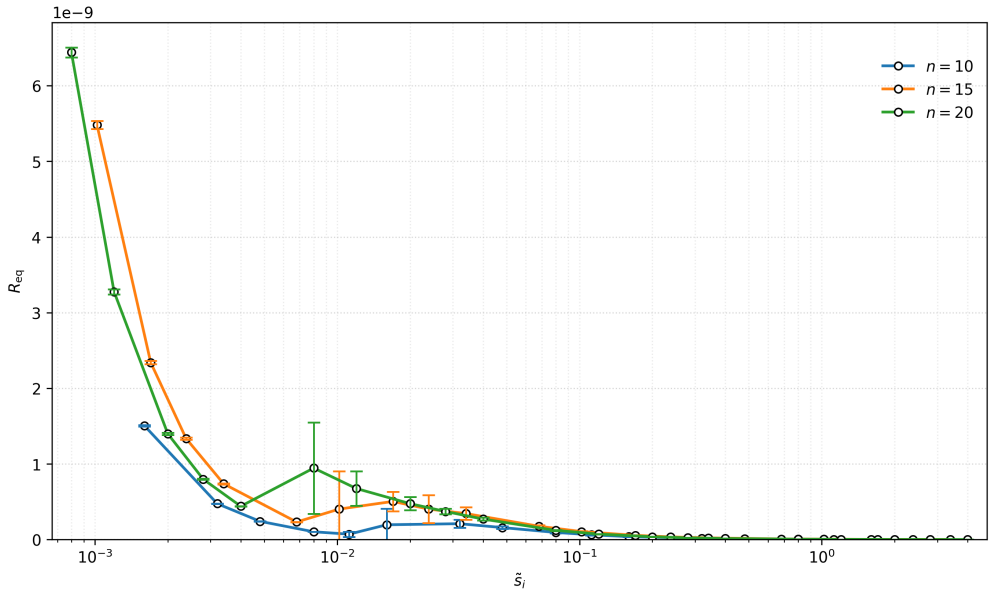

Figure 4.17: Equivalent resistance R_{eq} versus normalized sink $\tilde{s}_i$ for multiple grid sizes n. Error bars show the 95% confidence intervals across simulation seeds.

4.4.2 Fixed-radii sweep

We now turn to the rigid sweep protocol, in which the radius field is frozen to that obtained from a laminar optimization at the reference demand (see Section 3.4). Representative regime maps are shown in Fig. 4.18. As in the re-optimized case, turbulence first appears near the source and then propagates downstream as demand increases, following the same hierarchical pattern dictated by flow magnitude.

The turbulent fraction $\phi_{\text{turb}}(\tilde{s}_i)$, shown in Fig. 4.19, again displays a smooth growth and a good collapse across grid sizes.

In contrast, the equivalent resistance behaves qualitatively differently. As shown in Fig. 4.20, R_{eq} increases monotonically with $\tilde{s}_i$ when radii are held fixed. In this case, the progressive activation of turbulent segments leads to a steady increase in hydraulic losses, unmitigated by any compensating geometric reorganization.

Group	**Quantity**	**Symbol**	**Value**
Geometry	Edge length	L_{ij}	1.0 m
Fluid	Gravity	g	9.81 $\mathrm{m\,s^{-2}}$
	Kinematic viscosity	ν	1.0 $\mathrm{m^2\,s^{-1}}$
	Dynamic viscosity	μ	1.0 Pa s
	Density	ρ	$\mu/\nu = 1$ $\mathrm{kg\,m^{-3}}$
	Specific weight	γ_f	$g\,\rho = 9.81$ $\mathrm{N\,m^{-3}}$
Friction	Turbulent factor (eq. radius)	f	$5{\cdot}10^{-3}$
Mixed regime	Reynolds threshold	Re_c	4000
	Saturation threshold	ϕ_{sat}	0.99
Cost function*	Metabolic factor	b	1.0
	Maintenance exponent (fixed)	γ	0.5

Table 4.4: Model, regime, and optimization parameters used in the rigid sweep after one laminar optimization. *The cost function parameters refer to the laminar pre-optimization

Overall, the comparison between the two protocols shows that while the onset and spatial progression of turbulence are robust features of the flow, the global transport response of the network, as captured by R_{eq}, is highly sensitive to whether structural adaptation is allowed during the transition.

Turbulence consistently emerges first on the largest–radius edges, near the source. In both setups, the growth of the turbulent fraction $\phi_{\text{turb}}(\tilde{s}_i)$ is consistent across grid sizes n and broadly similar between the two protocols. The equivalent resistance, however, behaves very differently: with re-optimization $R_{\text{eq}}(\tilde{s}_i)$ shows a vaguely Moody-like, non-monotonic trend, whereas with fixed radii it increases monotonically. Differences in parameters between the two experimental setups (e.g., ν, ρ) may also contribute to this contrast and warrant further checking.

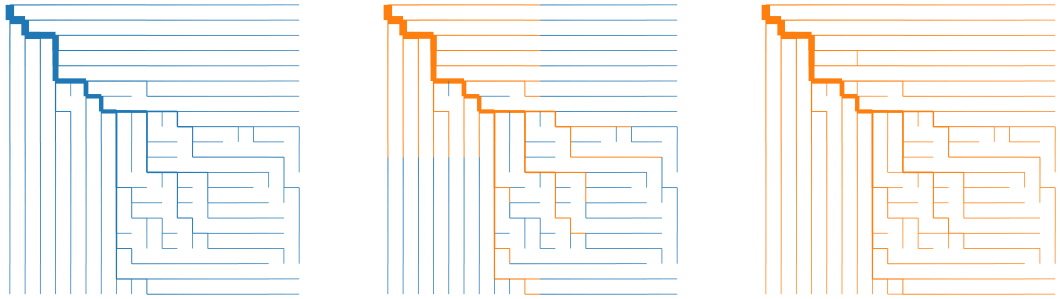

(a) Small s_0. (b) Medium s_0. (c) Large s_0.

Figure 4.18: Active edges colored by flow regime, for the fixed-radii sweep: laminar edges ($\alpha = 1$) are shown in blue, while turbulent edges ($\alpha = 0.5$) are shown in orange.

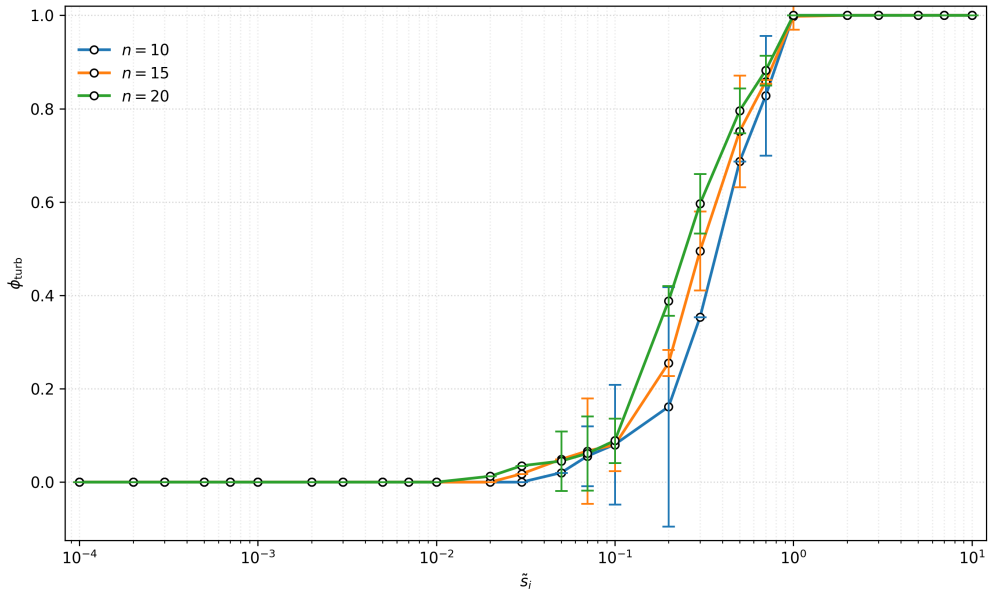

Figure 4.19: Turbulent fraction ϕ_{turb} versus normalized sink $\tilde{s}_i$ for multiple grid sizes n.

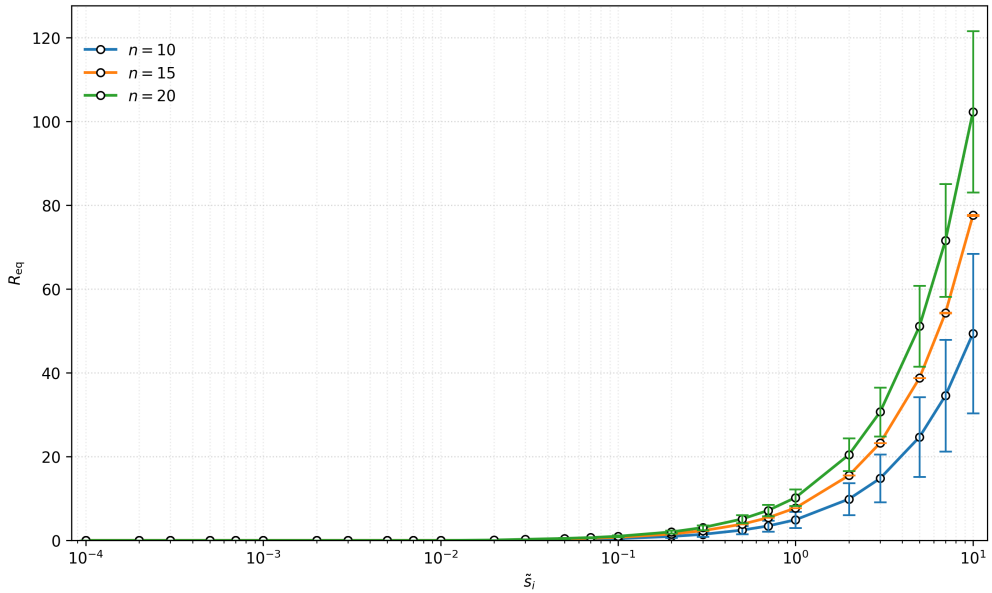

Figure 4.20: Equivalent resistance R_{eq} versus normalized sink $\tilde{s}_i$ for multiple grid sizes n. Error bars show the 95% confidence interval across seeds.

4.5 Discussion

This chapter explored how hydraulic physics (through the constitutive exponent α) and maintenance modeling (through the maintenance exponent γ) influence the structure and statistics of optimized transport networks. The numerical experiments were designed as controlled comparisons: all optimization settings were kept fixed while varying either the hydraulic regime assignment (laminar, turbulent, mixed) or the maintenance rule (constant $\gamma = \frac{1}{2}$ versus $\gamma(Q)$).

A first robust outcome is that, for the baseline parameter set (Tab. 4.1), the optimization procedure converges reliably in all configurations. Objective and dissipation traces decrease together and stabilize, and the accompanying stabilization of mean and variability of Re and τ_w indicates that the converged networks correspond to consistent hydraulic states rather than to transient numerical artifacts (Figs. 4.1–4.3). The residual oscillations observed in the mixed case are naturally explained by edges hovering near the threshold Re_c and being intermittently reclassified.

Regarding topology, the dominant control is exerted by the maintenance model. With concave maintenance ($\gamma = \frac{1}{2}$), the optimal architecture is tree-like in all three hydraulic scenarios, consistent with the concave costs picture. Introducing the flow-dependent rule $\gamma(Q)$ produces systematic departures from strict trees: the solutions remain organized around a main backbone, but small peripheral loops appear, typically in low-flow regions. In contrast, changing the hydraulic regime from laminar to turbulent has only a minor impact on the large-scale connectivity of the optimum: within each maintenance model examined, the three regimes produce networks that are visually and topologically very

similar (Fig. 4.4). This suggests that, under the present forcing and parameter choices, γ primarily selects the global architecture, while α mostly modulates local hydraulic fields on top of that architecture.

This separation of roles is also reflected in the global statistics. The edgewise distributions of Q are highly skewed in all cases and exhibit similar scaling exponents across regimes. Reynolds statistics broadly mirror those of Q in laminar and mixed settings, while the turbulent scenario displays a somewhat broader spread. The strongest regime-dependent signature appears in the wall shear stress distributions: under constant maintenance the mixed case is bimodal, reflecting the coexistence of laminar and turbulent edges, whereas the laminar and turbulent cases produce comparatively narrower and broader supports, respectively. When $\gamma(Q)$ is used, the τ_w distributions broaden in all regimes, consistent with an increase of heterogeneity induced by the adaptive maintenance rule (Figs. 4.7–4.14 and Tab. 4.2).

A key limitation of the baseline runs is that the fully turbulent closure ($\alpha = \frac{1}{2}$) is applied in a regime where most edges remain at low Reynolds numbers. In this situation the turbulent law can effectively underestimate hydraulic penalties, explaining both the lower converged objective in the "fully turbulent" case and the apparently reduced wall shear stress on edges labeled turbulent. These outcomes should therefore be read as model-dependent consequences of the adopted closure, rather than as physical predictions.

The demand-sweep experiments were introduced precisely to probe a more meaningful mixed-regime transition by spanning a wider Reynolds range with dedicated parameter sets. Two conclusions emerge. First, turbulence appears hierarchically: it is consistently triggered on large-radius, near-source edges and then propagates downstream as demand increases, and the turbulent fraction $\phi_{\mathrm{turb}}(\tilde{s}_i)$ shows a good collapse across grid sizes in both protocols, indicating that the ordering of transitions is robust and primarily controlled by local Reynolds thresholds. Second, the global transport response, summarized by the equivalent resistance R_{eq}, is highly protocol-dependent. When the network is re-optimized at each demand, geometric adaptation can partially compensate for the increasing share of turbulent edges, leading to a weakly non-monotonic trend. When radii are held fixed, no such compensation is available and R_{eq} increases monotonically with throughput. This contrast highlights that a mixed-regime transition cannot be interpreted purely as a change of local dissipation law: the possibility of morphological adaptation is an essential ingredient in determining the network's performance.

Overall, these results support the following qualitative picture. Concave maintenance selects tree-like backbones and largely fixes the global flow hierarchy; allowing maintenance to depend on flow promotes loop formation in peripheral regions; and mixed laminar–turbulent transitions introduce strong signatures in wall shear stress statistics and in effective resistance. The next part of the thesis will exploit this separation between global architecture and local hydraulic fields to compare OTNs with deterministic binary trees, where topology is prescribed and scaling can be analyzed analytically.

Part II

Deterministic Binary Trees

Chapter 5

Deterministic binary tree model

Deterministic binary trees are idealized transport networks in which the geometry and topology are prescribed *a priori*, rather than emerging from an optimization process. Their perfect symmetry and hierarchical structure make them analytically tractable and allow explicit derivations of hydraulic scalings across generations.

Such tree models are commonly employed as minimal representations of branching systems in both natural and engineered contexts, including vascular networks, plant hydraulics, and drainage structures. Variants of these models have been studied in literature in connection with optimal branching laws and fractal microchannel networks [Franco et al., 2006, Kou et al., 2014, Jing et al., 2018]. In contrast to optimized transport networks (Part I), deterministic trees isolate the effect of branching geometry and flow regime from adaptive morphological processes.

In this part of the thesis, deterministic binary trees are used as a theoretical benchmark to analyze wall shear stress scalings, head losses, and mixed-regime transitions in a setting where topology and geometry are fixed. This separation allows a transparent interpretation of global resistance measures and enables a comparison with the optimized networks discussed earlier.

5.1 Geometry and scaling

We consider a perfectly symmetric, deterministic binary tree composed of $m+1$ hierarchical levels, indexed by $k = 0,1,\ldots,m$, with the root located at level $k = 0$, following the construction introduced in Franco et al. [2006]. Each parent branch bifurcates into two identical daughter branches, so that the number of segments at level k is

$$N_k = 2^k.$$

All branches at the same level share identical geometric and hydraulic properties.

Branch geometry is prescribed through level-wise scaling laws for length and radius,

$$l_k = l_0\,\rho_L^{-k}, \qquad a_k = a_0\,\rho_A^{-k}, \tag{5.1}$$

where $\rho_L \geq 1$ and $\rho_A \geq 1$ denote the reduction ratios of length and radius between successive generations.

A total discharge Q is injected at the root and conserved throughout the tree. By symmetry, the volumetric flow rate carried by each branch at level k is

$$q_k = \frac{Q}{2^k}. \tag{5.2}$$

This hierarchical structure yields explicit expressions for flow rates, Reynolds numbers, pressure drops, and wall shear stresses as geometric progressions along the tree, enabling closed-form analysis under different flow regimes.

5.2 Hydraulic scalings along the tree

Thanks to its perfect symmetry, the deterministic binary tree admits explicit expressions for all relevant hydraulic quantities. At each generation, flow rates, velocities, Reynolds numbers, pressure drops, and wall shear stresses can be written in closed form and shown to follow simple geometric progressions. In this section we derive these scalings and show how they combine into compact global descriptors of the tree.

We begin by characterizing how the Reynolds number varies across generations, which allows us to distinguish laminar, turbulent, and mixed configurations. We then derive the corresponding level-wise head losses and show that the total pressure drop naturally decomposes into a linear and a quadratic contribution in the inlet discharge. Finally, we analyze the resulting wall shear stress profiles and relate them to classical optimality conditions.

5.2.1 Reynolds number and flow regimes

At level k, each branch can be treated as a straight circular pipe carrying a volumetric flow rate q_k and having radius a_k. The local Reynolds number is therefore defined as

$$Re_k = \frac{\rho U_k D_k}{\mu}, \tag{5.3}$$

where $U_k = q_k/(\pi a_k^2)$ is the mean velocity and $D_k = 2a_k$ the diameter. Substituting these expressions gives

$$Re_k = \frac{\rho}{\mu}\frac{q_k}{\pi a_k^2}(2a_k) = \frac{2\rho}{\pi\mu}\frac{q_k}{a_k}. \tag{5.4}$$

Using the geometric relations $q_k = Q/2^k$ and $a_k = a_0\rho_A^{-k}$, the Reynolds number can be written explicitly as a function of the generation index,

$$Re_k = Re_0\left(\frac{\rho_A}{2}\right)^k, \qquad Re_0 = \frac{2\rho}{\pi\mu}\frac{Q}{a_0}. \tag{5.5}$$

Thus, Re_k varies geometrically along the tree. Depending on the diameter ratio ρ_A, it may decrease toward the leaves, remain constant, or increase downstream.

To account for the possible coexistence of laminar and turbulent segments, we introduce a critical Reynolds number Re_c and define the level sets

$$\mathcal{L} = \{k : Re_k < Re_c\}, \qquad \mathcal{T} = \{k : Re_k \geq Re_c\}. \tag{5.6}$$

Depending on the diameter ratio ρ_A, it may decrease toward the leaves, remain constant, or increase downstream.

Role of the ratio $\rho_A/2$: proximal vs distal transition. Equation (5.5) shows that the ordering of local Reynolds numbers across generations is entirely controlled by the factor $\rho_A/2$. If $\rho_A < 2$, then $(\rho_A/2) < 1$ and Re_k decreases with k, so proximal branches reach any critical threshold first and turbulence (when present) invades the tree from the root toward the leaves as Re_0 increases. If $\rho_A = 2$, then Re_k is independent of k and the transition is simultaneous across the entire tree. Finally, if $\rho_A > 2$, then $(\rho_A/2) > 1$ and Re_k increases with k, so distal branches become turbulent first and turbulence propagates backward toward the root.

To account for the possible coexistence of laminar and turbulent segments, we introduce a critical Reynolds number Re_c and define the level sets

$$\mathcal{L} = \{k : Re_k < Re_c\}, \qquad \mathcal{T} = \{k : Re_k \geq Re_c\}. \tag{5.7}$$

Since Re_k is monotone in k for $\rho_A \neq 2$, there exists at most one transition generation separating laminar and turbulent subtrees. As a result, a tree can be fully laminar, fully turbulent, or exhibit a mixed configuration.

5.2.2 Level-wise head losses and global decomposition

Once the flow regime at each level is identified, the corresponding pressure drop along a branch can be computed using the appropriate constitutive law.

Laminar branches. For levels belonging to $\mathcal{L}$, the flow is assumed to be Poiseuille. The pressure drop along a branch at level k is then

$$\Delta p_k^{(\mathrm{lam})} = \frac{8\mu\, l_k}{\pi a_k^4}\, q_k, \qquad k \in \mathcal{L}. \tag{5.8}$$

Fully rough turbulent branches. For levels in $\mathcal{T}$, we assume fully rough turbulent flow with a Reynolds-independent Darcy friction factor f. The Darcy–Weisbach law yields

$$\Delta p_k^{(\mathrm{turb})} = \frac{f\rho\, l_k}{4\pi^2 a_k^5}\, q_k^2, \qquad k \in \mathcal{T}. \tag{5.9}$$

Total head loss. Along any root-to-leaf path, branches are connected in series and there is no leakage. The total root-to-leaf head loss of the tree therefore results from summing the contributions of all generations,

$$\Delta P = \sum_{k\in\mathcal{L}} \Delta p_k^{(\mathrm{lam})} + \sum_{k\in\mathcal{T}} \Delta p_k^{(\mathrm{turb})}. \tag{5.10}$$

Using $q_k = Q/2^k$, this expression can be rearranged into the compact form

$$\Delta P = A_L\, Q + A_T\, Q^2, \tag{5.11}$$

where the coefficients

$$A_L = \sum_{k\in\mathcal{L}} \frac{8\mu\, l_k}{\pi a_k^4\, 2^k}, \qquad A_T = \sum_{k\in\mathcal{T}} \frac{f\rho\, l_k}{4\pi^2 a_k^5\, 4^k} \tag{5.12}$$

collect the laminar and turbulent contributions, respectively. This linear–quadratic decomposition in Q will play a central role in the definition of equivalent single-pipe descriptors.

5.2.3 Wall shear stress scalings

The wall shear stress provides a local measure of the mechanical load exerted by the flow on the conduit walls. For a straight circular pipe of length l_k and diameter $D_k = 2a_k$, it is related to the pressure drop through

$$\tau_{w,k} = \frac{\Delta p_k\, D_k}{4\, l_k}. \tag{5.13}$$

Laminar regime. Substituting the laminar pressure drop (5.8) into (5.13) yields

$$\tau_{w,k}^{(\mathrm{lam})} = \frac{4\mu}{\pi}\,\frac{q_k}{a_k^3} = \frac{4\mu Q}{\pi a_0^3}\left(\frac{\rho_A^3}{2}\right)^k. \tag{5.14}$$

Thus, in laminar flow the wall shear stress varies geometrically along the tree, with a ratio controlled solely by the diameter scaling ρ_A.

Fully developed turbulent regime on rough walls. Using the turbulent pressure drop (5.9) gives

$$\tau_{w,k}^{(\mathrm{turb})} = \frac{f}{8}\,\rho\, U_k^2 = \frac{f\rho Q^2}{8\pi^2 a_0^4}\left(\frac{\rho_A^4}{4}\right)^k, \tag{5.15}$$

where $U_k = q_k/(\pi a_k^2)$. Notably, the length ratio ρ_L does not appear in these expressions, reflecting the fact that wall shear stress is governed by local momentum balance rather than by axial extent.

Constancy of wall shear stress. From Eqs. (5.14) and (5.15),

$$\tau_{w,k}^{(\mathrm{lam})} \propto \left(\frac{\rho_A^3}{2}\right)^k, \qquad \tau_{w,k}^{(\mathrm{turb})} \propto \left(\frac{\rho_A^4}{4}\right)^k,$$

so the wall shear stress is uniform across generations only for the critical ratios

$$\boxed{\rho_A = 2^{1/3}\ \text{(laminar)}, \qquad \rho_A = \sqrt{2}\ \text{(turbulent, rough walls)}}.$$

Relation to optimality. In the laminar regime, the constant-shear condition $\rho_A = 2^{1/3}$ coincides with the classical Murray ratio that minimizes hydraulic resistance under a fixed-volume constraint [Kou et al., 2014, Lu and Kou, 2022]. In contrast, for fully rough turbulent flow the constant-shear ratio $\rho_A = \sqrt{2}$ differs from the resistance-optimal value $\rho_A^* = 2^{3/7}$ [Kou et al., 2014]. This mismatch highlights the fundamental difference between uniform wall loading and minimal dissipation in turbulent branching networks.

5.3 Equivalent pipe representation

Although the deterministic tree admits explicit level-wise expressions, it is often convenient to summarize its global hydraulic behavior through a single effective descriptor. To this end, we introduce an equivalent straight pipe that reproduces the same total head loss as the branching network under the same inlet discharge. This construction provides a natural bridge between the tree geometry and classical pipe-flow concepts, and will allow us to define global friction laws in direct analogy with the Moody diagram.

Notation. Throughout this section, lowercase symbols with subscripts denote quantities defined at the level of individual branches in the tree $(l_k, a_k, q_k, \Delta p_k)$, while uppercase symbols denote the corresponding quantities associated with the equivalent single conduit $(L, D, U, \Delta P)$.

Equivalent geometry. The equivalent pipe is defined operationally by requiring that it dissipates the same total head loss ΔP as the branching tree when carrying the same inlet discharge Q. The emergence of a Moody-like behavior at the network level mirrors classical results obtained for branching systems and equivalent-pipe representations [Kou et al., 2014]. Since all root-to-leaf paths are hydraulically equivalent by symmetry, the global pressure drop of the tree can be represented by a single path composed of branches connected in series.

Accordingly, the axial length of the equivalent pipe is defined as the series sum of all branch lengths along a root-to-leaf path,

$$L = \sum_{k=0}^{m} l_k = l_0 \, \frac{1 - \rho_L^{-(m+1)}}{1 - \rho_L^{-1}}. \tag{5.16}$$

This choice reflects the fact that, hydraulically, the tree behaves as a sequence of resistive elements connected in series without leakage.

To fix the diameter of the equivalent pipe, we impose conservation of the total material volume. The total volume of the branching network is

$$V = \sum_{k=0}^{m} 2^k \, \pi a_k^2 \, l_k, \tag{5.17}$$

and equating this to the volume of the equivalent pipe yields

$$V = \frac{\pi D^2}{4} L \quad \rightarrow \quad D = \left(\frac{4V}{\pi L} \right)^{1/2}. \tag{5.18}$$

Once the equivalent geometry is fixed, the mean velocity and the associated Reynolds number follow directly as

$$U = \frac{4Q}{\pi D^2}, \qquad Re_{eq} = \frac{\rho U D}{\mu}. \tag{5.19}$$

5.4 Equivalent friction factor

With the equivalent geometry defined, we can characterize the global hydraulic response of the tree through an effective Darcy–Weisbach friction factor. The equivalent friction factor f_{eq} is defined by enforcing the standard pipe relation

$$\Delta P = f_{eq} \frac{L}{D} \frac{\rho U^2}{2}, \tag{5.20}$$

with ΔP equal to the total head loss of the branching network.

Using the decomposition $\Delta P = A_L Q + A_T Q^2$ derived in Section 5.2.2, together with $U = 4Q/(\pi D^2)$, one obtains

$$f_{eq} = \frac{\pi^2 D^5}{8\rho L} \left(\frac{A_L}{Q} + A_T \right). \tag{5.21}$$

Expressing the discharge in terms of the equivalent Reynolds number finally leads to a Moody-type law,

$$f_{eq}(Re_{eq}) = C_T + \frac{C_L}{Re_{eq}}, \qquad C_T = \frac{\pi^2 D^5}{8\rho L} A_T, \quad C_L = \frac{\pi D^4}{2\mu L} A_L. \tag{5.22}$$

This result shows that a branching tree operating under mixed laminar and fully rough turbulent conditions behaves, at the global scale, as an equivalent pipe whose friction factor combines a laminar $1/Re$ decay with a turbulent plateau, closely mirroring the structure of the classical Moody diagram.

5.5 Dimensionless mixed resistance

In a branching tree operating under mixed flow regimes, different generations contribute to the total head loss through fundamentally different constitutive laws: linear in the discharge for laminar segments and quadratic for turbulent ones. As a consequence, the global resistance of the network cannot be described by a single coefficient without further processing.

In this section we construct a dimensionless mixed resistance that quantifies the relative hydraulic cost of the laminar and turbulent portions of the tree in a unified and physically consistent manner.

Level-wise resistance coefficients

At each level k, the pressure drop can be expressed in terms of a resistance coefficient whose form depends on the local flow regime,

$$\Delta p_k = \begin{cases} R_k^{(\mathrm{L})}\, Q, & k \in \mathcal{L}, \\ R_k^{(\mathrm{T})}\, Q^2, & k \in \mathcal{T}. \end{cases} \tag{5.23}$$

Using the expressions for Poiseuille and Darcy–Weisbach losses, the corresponding level-wise coefficients are

$$R_k^{(\mathrm{L})} = \frac{8\mu\, l_k}{\pi a_k^4\, 2^k}, \qquad R_k^{(\mathrm{T})} = \frac{f\,\rho\, l_k}{4\pi^2 a_k^5\, 4^k}. \tag{5.24}$$

Cumulative laminar and turbulent contributions

Summing the level-wise coefficients over the laminar and turbulent subsets yields the cumulative resistance coefficients

$$R_{\mathrm{L}} = \sum_{k\in\mathcal{L}} R_k^{(\mathrm{L})}, \qquad R_{\mathrm{T}} = \sum_{k\in\mathcal{T}} R_k^{(\mathrm{T})}. \tag{5.25}$$

At this stage, however, R_{L} and R_{T} cannot be combined directly. The two coefficients have different physical dimensions,

$$[R_k^{(\mathrm{L})}] = \mathrm{Pa\,s\,m^{-3}}, \qquad [R_k^{(\mathrm{T})}] = \mathrm{Pa\,s^2\,m^{-6}},$$

reflecting the fundamentally different scaling of laminar and turbulent losses with discharge. A meaningful mixed resistance therefore requires a suitable normalization of each contribution.

Reference single-pipe resistances

To construct dimensionless measures, we introduce two reference pipes, one for the laminar subnetwork and one for the turbulent subnetwork. Each reference pipe is defined by conserving the total length and volume of the corresponding subset of the tree.

Laminar reference pipe. The laminar subnetwork is characterized by the total length

$$L_s^{(\mathrm{L})} = \sum_{k\in\mathcal{L}} l_k, \tag{5.26}$$

and total volume

$$V_s^{(\mathrm{L})} = \sum_{k\in\mathcal{L}} 2^k\, \pi a_k^2\, l_k. \tag{5.27}$$

Imposing volume conservation defines the equivalent diameter

$$D_s^{(\mathrm{L})} = \left(\frac{4V_s^{(\mathrm{L})}}{\pi L_s^{(\mathrm{L})}} \right)^{1/2}, \tag{5.28}$$

and the corresponding laminar single-pipe resistance

$$R_s^{(\mathrm{L})} = \frac{128\,\mu\,L_s^{(\mathrm{L})}}{\pi D_s^{(\mathrm{L})4}}. \tag{5.29}$$

Turbulent reference pipe. Analogously, the turbulent subnetwork has total length

$$L_s^{(\mathrm{T})} = \sum_{k\in\mathcal{T}} l_k, \tag{5.30}$$

and total volume

$$V_s^{(\mathrm{T})} = \sum_{k\in\mathcal{T}} 2^k\,\pi a_k^2\,l_k. \tag{5.31}$$

The equivalent diameter follows as

$$D_s^{(\mathrm{T})} = \left(\frac{4V_s^{(\mathrm{T})}}{\pi L_s^{(\mathrm{T})}}\right)^{1/2}, \tag{5.32}$$

and the rough-turbulent resistance coefficient is

$$R_s^{(\mathrm{T})} = \frac{8\,f\,\rho\,L_s^{(\mathrm{T})}}{\pi^2 D_s^{(\mathrm{T})5}}. \tag{5.33}$$

Dimensionless mixed resistance

Each cumulative contribution can now be normalized by its corresponding reference resistance,

$$R_{\mathrm{L}}^{+} = \frac{R_{\mathrm{L}}}{R_s^{(\mathrm{L})}}, \qquad R_{\mathrm{T}}^{+} = \frac{R_{\mathrm{T}}}{R_s^{(\mathrm{T})}}. \tag{5.34}$$

We finally define the total dimensionless mixed resistance as

$$R_{\mathrm{mix}}^{+} = R_{\mathrm{L}}^{+} + R_{\mathrm{T}}^{+}. \tag{5.35}$$

This construction extends the Kou et al. [2014] formulation to deterministic branching networks operating under mixed laminar and turbulent flow regimes, and provides a compact scalar measure of their global hydraulic cost.

Chapter 6

Numerical Results on Deterministic Binary Trees

This chapter presents numerical results obtained for deterministic binary trees, with the aim of validating the analytical scalings derived in Chapter 5 and illustrating how mixed laminar–turbulent configurations emerge as the inlet Reynolds number increases. Particular attention is devoted to the behavior of global equivalent descriptors, such as the equivalent friction factor and the dimensionless mixed resistance, and to their connection with local flow-regime transitions across generations.

6.1 Setup of the numerical sweep

We consider a deterministic binary tree composed of $m = 6$ hierarchical levels, with geometric scaling parameters

$$\rho_A = 2^{1/3}, \qquad \rho_L = 1.1.$$

The choice $\rho_A = 2^{1/3}$ corresponds to the Murray scaling, which ensures constant wall shear stress in the laminar regime and provides a natural reference configuration. Since $\rho_A = 2^{1/3} < 2$, Eq. (5.5) implies that Re_k decreases with k, so turbulence (when it occurs) appears first in proximal generations and then propagates toward the leaves as Re_0 increases.

A sweep is performed over the inlet Reynolds number Re_0, defined at the root level as in Eq. (5.5), while keeping all geometric parameters fixed. For each value of Re_0, the local Reynolds numbers Re_k are evaluated along the tree and each level is classified as laminar or turbulent according to the threshold Re_c introduced in Chapter 5.

The numerical sweep allows us to explore fully laminar, mixed, and fully turbulent configurations within a single, fixed geometry.

6.2 Local flow fields and global descriptors

For each value of the inlet Reynolds number Re_0, we evaluate both local and global hydraulic quantities on the tree. At the local scale, we compute the Reynolds number Re_k and the corresponding wall shear stress $\tau_{w,k}$ at each generation. At the global scale, we extract the equivalent Darcy–Weisbach friction factor $f_{\mathrm{eq}}(Re_0)$ and the dimensionless mixed resistance $R^{+}_{\mathrm{mix}}(Re_0)$, as defined in Chapter 5.

Figure 6.1 illustrates three representative configurations corresponding to increasing inlet Reynolds numbers Re_0: a fully laminar regime, an intermediate mixed laminar–turbulent regime, and a fully turbulent regime. The sequence highlights how the transition to turbulence propagates hierarchically from proximal to distal levels as the global throughput increases.

The local flow fields shown in Fig. 6.1 can be summarized into global hydraulic descriptors by mapping the entire branching structure onto an equivalent single conduit. Figure 6.2 reports the resulting equivalent Darcy friction factor f_{eq} and the dimensionless mixed resistance R^{+}_{mix} as functions of the inlet Reynolds number Re_0, providing a compact, network-scale characterization of the laminar–turbulent transition.

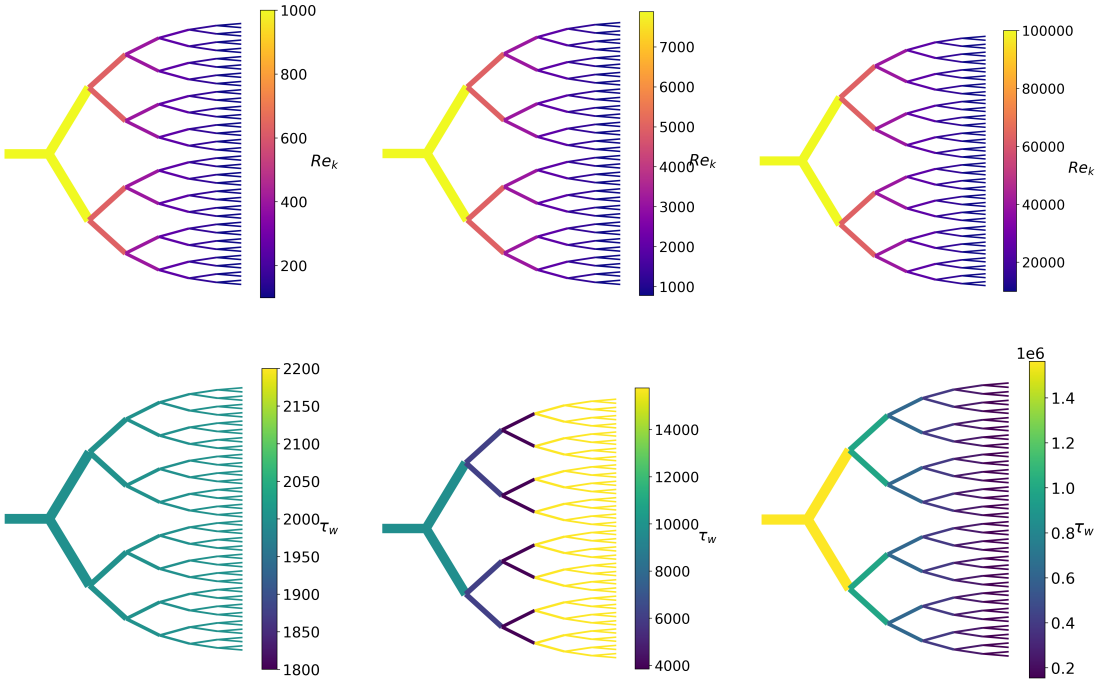

Figure 6.1: Local Reynolds numbers (top row) and wall shear stresses (bottom row) for three representative inlet Reynolds numbers Re_0.

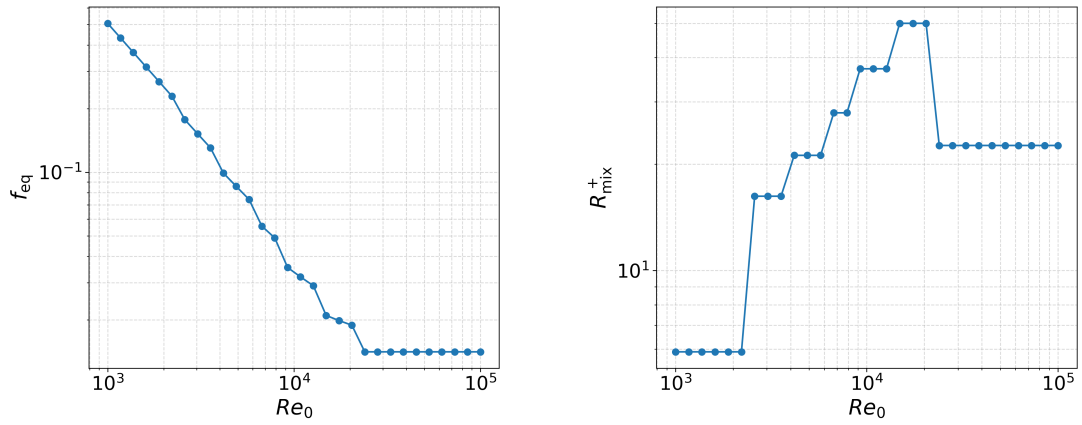

Figure 6.2: Global equivalent descriptors as functions of the inlet Reynolds number Re_0. Left: equivalent Darcy–Weisbach friction factor $f_{eq}(Re_0)$. Right: dimensionless mixed resistance $R^+_{mix}(Re_0)$.

6.3 Discussion

The numerical sweep on the deterministic binary tree reveals a clear and structured transition of the global hydraulic behavior as the inlet Reynolds number Re_0 increases.

At low Re_0, all levels remain in the laminar regime. The maps of local Reynolds numbers display a smooth geometric decay along successive generations, and the wall shear stress is nearly uniform across the tree, consistently with the analytical prediction for the Murray scaling $\rho_A = 2^{1/3}$.

As Re_0 increases, the proximal branches exceed the critical Reynolds number while distal levels remain laminar, giving rise to mixed laminar–turbulent configurations. This transition is clearly visible in both the Reynolds and wall-shear maps, where a sharp contrast develops between turbulent upstream levels and laminar downstream ones.

The global equivalent friction factor f_{eq} exhibits a classical Moody-type behavior: an initial laminar branch with $f_{eq} \sim Re_0^{-1}$, followed by a transition region in which laminar and turbulent contributions coexist, and finally a plateau corresponding to the fully rough turbulent regime.

In contrast, the dimensionless mixed resistance R^+_{mix} displays a sequence of discrete jumps as Re_0 increases. Each jump corresponds to the activation of a new turbulent level, reflecting the hierarchical structure of the tree. Once all levels become turbulent, R^+_{mix} saturates to a constant value, as the normalized rough-turbulent contribution dominates.

Overall, these numerical results confirm that a deterministic branching tree operating under mixed flow regimes behaves, at the global scale, as an equivalent pipe whose friction law is the superposition of laminar and rough–turbulent contributions, in full agreement with the analytical framework developed in Chapter 5.

Conclusions

This thesis studied fluid transport on networks within a unified graph-based hydraulic framework, with the specific goal of understanding how flow regime, geometry, and adaptation mechanisms interact to shape global transport properties. Rather than aiming at a detailed physical description of a specific system, the work deliberately focused on simplified and controlled settings, allowing the role of individual modeling ingredients to be isolated and compared.

Two complementary classes of networks were investigated. Optimized transport networks (OTNs) were used to explore how network structure emerges from the minimization of a global cost functional, while deterministic binary trees provided analytically tractable reference systems in which geometry and topology are fixed *a priori*. Studying both settings within the same hydraulic formalism made it possible to disentangle the effects of optimization from those imposed purely by branching geometry and flow physics.

Optimized transport networks

In optimized transport networks, the results consistently show that the maintenance model is the primary determinant of large-scale topology. For a concave maintenance cost with constant exponent $\gamma = \frac{1}{2}$, optimal configurations are strictly tree-like, independently of the hydraulic regime. Allowing the maintenance exponent to depend on the flow, $\gamma(Q)$, induces the appearance of peripheral loops while preserving a dominant tree-like backbone.

By contrast, changing the constitutive flow exponent from laminar ($\alpha = 1$) to turbulent ($\alpha = \frac{1}{2}$), or allowing a mixed edgewise assignment, has only a secondary impact on network connectivity. Within a given maintenance model, laminar, turbulent, and mixed networks are topologically very similar. This separation of roles indicates that, in the present setup, maintenance costs select the global architecture, while hydraulic physics mainly modulates local quantities such as flow intensity, Reynolds number, and wall shear stress.

This picture is reinforced by the statistical analysis. Flow distributions are strongly heterogeneous and exhibit similar scaling behavior across regimes, whereas wall shear stress distributions carry the clearest signature of the hydraulic closure. In particular, mixed laminar–turbulent networks display bimodal stress distributions, directly reflecting the coexistence of different dissipation mechanisms on distinct edges.

Demand-sweep experiments further highlight the distinction between local regime transitions and global network response. Laminar–turbulent transitions occur hierarchically,

with turbulence appearing first on high-flow, near-source edges and propagating downstream as demand increases. Although the order in which different branches transition from laminar to turbulent flow is robust, the impact of these transitions on the equivalent resistance depends sensitively on whether the network geometry is fixed or adaptive. Re-optimized networks can compensate for the onset of turbulence through geometric reorganization, whereas networks with fixed radii exhibit a monotonic increase of resistance with throughput.

Deterministic binary trees

Deterministic binary trees provide a complementary perspective, in which the effects of branching geometry and flow regime can be analyzed without the additional complexity of optimization. Thanks to their perfect symmetry, explicit expressions were derived for Reynolds numbers, pressure drops, and wall shear stresses along successive generations.

The analysis highlights the central role of diameter scaling. In the laminar regime, the Murray ratio $\rho_A = 2^{1/3}$ ensures uniform wall shear stress across generations. In fully rough turbulent flow, the corresponding constant-shear condition becomes $\rho_A = \sqrt{2}$, which differs from the resistance-optimal scaling for turbulent pipes $\rho_A^* = 2^{3/7}$. This mismatch emphasizes that uniform mechanical loading and minimal dissipation are not equivalent optimality principles in turbulent branching networks.

A key outcome of the tree analysis is the decomposition of the total head loss into laminar and turbulent contributions that scale linearly and quadratically with the inlet discharge. This structure naturally leads to an equivalent pipe representation, whose friction factor follows a Moody-type law combining a $1/Re$ decay with a turbulent plateau. A dimensionless mixed resistance was also introduced to quantify the relative contribution of laminar and turbulent subtrees in a consistent manner.

Numerical sweeps over the inlet Reynolds number confirm the analytical predictions. Mixed configurations emerge through discrete, generation-by-generation transitions, which appear as stepwise changes in the mixed resistance, while the equivalent friction factor evolves smoothly.

Perspective and limitations

Taken together, the results of this thesis suggest a coherent and internally consistent picture. Deterministic trees clarify how branching geometry and flow regime alone shape global hydraulic descriptors, while optimized transport networks demonstrate how these descriptors are modified when geometry becomes an adaptive variable.

At the same time, the conclusions of this work must be interpreted within the limits of the adopted modeling choices. The Reynolds threshold used to distinguish laminar and turbulent edges is a pragmatic device rather than a representation of the physical onset of turbulence, and the fully rough turbulent closure is employed as a stylized nonlinear law, even outside its strict range of validity. Similarly, the forcing patterns and network geometries considered here are deliberately simple, allowing controlled comparisons at the expense of realism.

Within these limits, the thesis provides a coherent framework for analyzing transport networks across flow regimes and levels of structural adaptation, and establishes a clear connection between classical pipe flow concepts and network-level hydraulic behavior.

Bibliography

Jayanth R. Banavar, Francesca Colaiori, Alessandro Flammini, Amos Maritan, and Andrea Rinaldo. Topology of the fittest transportation network. *Physical Review Letters*, 84(20):4745–4748, 2000.

Francis Corson. Fluctuations and redundancy in optimal transport networks. *Physical Review Letters*, 104:048703, 2010.

Walfre Franco, Mihir Sen, and K. T. Yang. Flows in large, self-similar tree networks and their control. *Proceedings of the Royal Society A*, 462:2907–2926, 2006.

Luca Giaccone, Shashank Kumar Anand, Amilcare Porporato, and Luca Ridolfi. Coexistence of loop and tree structures in transport networks. *Physical Review E*, 111:014319, 2025.

Dalei Jing, Shiyu Song, Yunlu Pan, and Xiaoming Wang. Optimal fractal tree-like microchannel networks with slip for laminar-flow-modified murray's law. *Beilstein Journal of Nanotechnology*, 9:482–489, 2018.

Eleni Katifori, Gergely J. Szöllősi, and Marcelo O. Magnasco. Damage and fluctuations induce loops in optimal transport networks. *Physical Review Letters*, 104:048704, 2010.

Bowen Kou, David Elad, and Eran Bouchbinder. Optimal structure of tree-like branching networks for fluid flow. *Physical Review Letters*, 113:268101, 2014.

Hangjun Lu and Jianlong Kou. Equivalent resistance and flow properties of tree-like networks. *Journal of Hydrology*, 608:127631, 2022.

Henrik Ronellenfitsch and Eleni Katifori. Global optimization, local adaptation, and the role of growth in distribution networks. *Physical Review Letters*, 123:248101, 2019.